PIONEER AND INNOVATIVE STUDIES IN MECHANICAL ENGINEERING

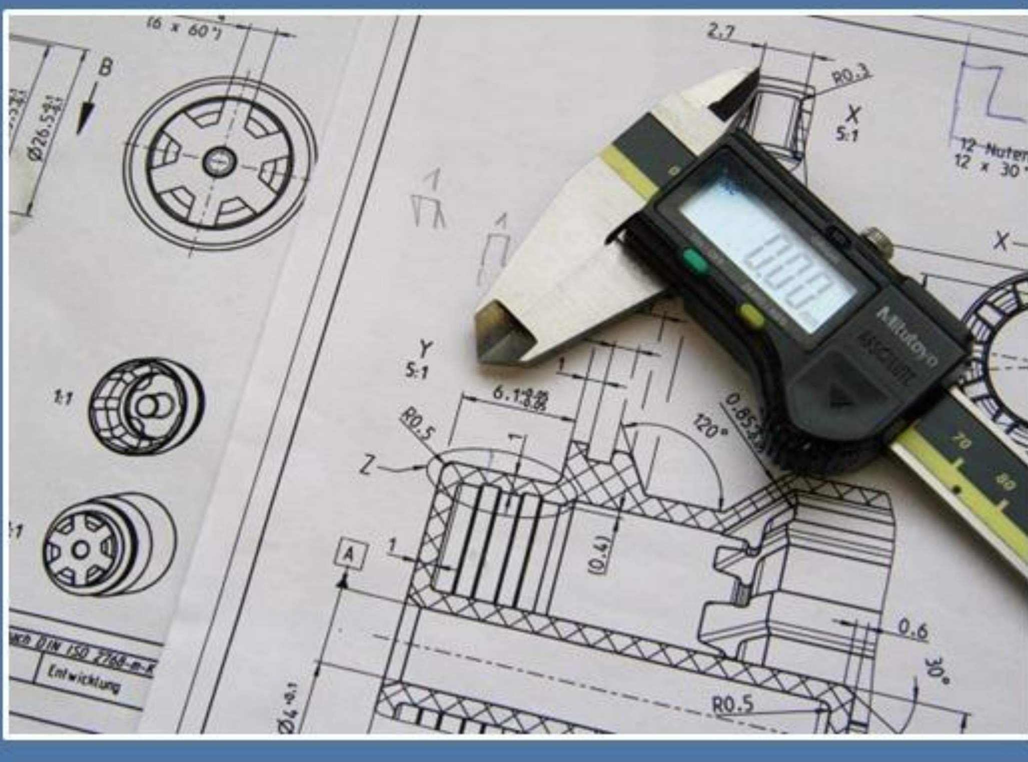

All Sciences Academy

PIONEER AND INNOVATIVE STUDIES IN MECHANICAL ENGINEERING

Editor
Prof. Dr. İSMET SEZER

Pioneer and Innovative Studies In Mechanical Engineering
Editor: Prof. Dr. İSMET SEZER

Design: All Sciences Academy Design
Published Date: December 2024
Publisher's Certification Number: 72273
ISBN: 978-625-5954-16-9

www.allsciencesacademy.com
allsciencesacademy@gmail.com

CONTENT

Modeling of Long-Term Global Solar Radiation for Mersin Province using Artificial Neural Networks

Fatih ÜNAL[1]
Merve Şentürk ACAR[2]
Bünyamin DEMİR[3]

1- Assoc. Prof. Dr.; Mersin University, Engineering Faculty, Department of Mechanical Engineering. fatihunal@mersin.edu.tr ORCID No: 0000-0001-6660-9984
2- Assoc. Prof. Dr.; Bilecik Şeyh Edebali University, Engineering Faculty, Department of Mechanical Engineering. merve.senturkacar@bilecik.edu.tr ORCID No: 0000-0003-1442-4560
3- Assoc. Prof. Dr.; Mersin University, Engineering Faculty, Department of Mechanical Engineering. bd@mersin.edu.tr ORCID No: 0000-0002-6405-4724

ABSTRACT

In this investigation, the phenomenon of global solar radiation was meticulously modeled utilizing artificial neural networks (ANNs), drawing upon a comprehensive dataset spanning a decade of solar radiation measurements within the Mersin province. Recognized for its considerable solar energy prospects, Mersin serves as an ideal locale for establishing a robust scientific framework for extended forecasting endeavors. During the modeling procedure, pivotal input variables such as solar altitude angle, wind speed, and dry-bulb temperature were employed, culminating in the direct solar radiation value as the output variable. The model's formulation was executed through the MATLAB Neural Fitting Tool (nfttool), wherein the dataset was systematically partitioned into 75% for training, 15% for validation, and 10% for testing purposes. A configuration featuring 30 neurons within the hidden layer was adopted, and the Levenberg-Marquardt backpropagation algorithm was implemented. This algorithm significantly bolstered the model's efficacy, facilitating rapid convergence alongside heightened accuracy. The findings underscored that the correlation coefficient (R) values exceeded 0.90 across both the training and testing datasets. Such elevated performance levels attest to the ANN's proficiency in effectively capturing nonlinear dynamics. This modeling endeavor not only provides a more adaptable and precise methodology for predicting solar radiation but also surpasses the limitations of conventional approaches. The inherent flexibility and accuracy afforded by this technique hold strategic implications for energy planning, solar power installation design, and the optimization of renewable energy initiatives. Particularly in locales characterized by abundant solar energy potential, such as the Mersin province, this ANN-centric modeling strategy emerges as a pivotal contributor to sustainable energy advancements.

Keywords –Global Solar Radiation, Artificial Neural Networks (ANNs), Levenberg-Marquardt Algorithm, Solar Energy Modeling, Mersin.

INTRODUCTION

As delineated within the present examination, the modeling of long-term global solar radiation specific to the Mersin province via artificial neural networks has been meticulously explored. This investigation underscores the paramount significance of accurately predicting solar radiation, a factor of critical relevance across a multitude of domains, including the optimized utilization of renewable energy resources, strategic energy planning, the operational efficiency of photovoltaic systems, and broader climate change assessments. The primary aim of this study is to intricately model the prolonged solar radiation data pertinent to the region through the application of artificial neural networks, thereby establishing a robust foundation for forthcoming energy strategies and scientific inquiries derived from the outcomes of this methodology. The proficiency of artificial neural networks in encapsulating nonlinear relationships inherent in solar radiation modeling confers a notable enhancement in accuracy relative to conventional methodologies. In a locale such as Mersin, characterized by its abundant solar energy potential, this innovative approach renders a substantial contribution towards the effective harnessing of energy resources and the augmentation of the region's renewable energy capabilities.

The prediction of solar radiation plays a pivotal role in enhancing the efficacy of renewable energy utilization and in assessing the potential of solar energy resources. Within this paradigm, methodologies leveraging artificial neural networks (ANNs) have emerged as a formidable alternative to conventional techniques, markedly improving accuracy metrics. In light of this, an extensive review of literature pertaining to the modeling of long-term global solar radiation specifically in the Mersin province has been conducted, emphasizing the diverse applications of ANNs alongside analogous techniques. In their seminal work, Voyant et al. (2010) scrutinized the efficacy of ANNs in forecasting solar radiation in remote locales, positing that a synergistic approach combining physical modeling with statistical methodologies can significantly enhance predictive precision. Likewise, Carles Martí Pérez and Gasque Albalate (2011) introduced an ANN-driven model for global radiation forecasting in regions lacking direct measurement apparatus, successfully augmenting the ANN's accuracy through the integration of ancillary data. Lauret et al. (2012) tackled the inherent non-stationarity present in solar radiation data series, endeavoring to derive stationary solar series via a Bayesian model committee, thereby contributing substantially to the field of time series analysis. Additionally, Bonanno et al. (2013) employed radial basis function neural networks (RBFNN) for the prediction of photovoltaic module electrical characteristics, achieving commendable outcomes under high irradiance conditions. In a similar vein, Yadav and Sethy (2018) underscored the significance of their developed ANN model for short-term solar radiation forecasting, particularly with respect to photovoltaic energy generation. Lastly, Ghazvinian et al. (2019) appraised a model predicated on support vector regression and particle swarm optimization, undertaking a comparative analysis of various ANN types, ultimately determining that radial basis neural networks yielded the most favorable results.

In recent explorations of methodologies for solar radiation forecasting, the convergence of data integration techniques and machine learning paradigms has garnered considerable attention. Notably, Ahmadi et al. (2020) undertook a comparative analysis of artificial neural networks (ANN) alongside various machine learning modalities to assess the thermal efficacy of photovoltaic-thermal solar collectors. In a parallel vein, Hoyos-Gómez et al. (2021) directed their efforts towards the short-term forecasting of global solar radiation amid conditions of incomplete data, achieving commendable outcomes through the application of time series analytics. Furthermore, Ordoñez Palacios et al. (2022) innovatively crafted a machine learning framework that amalgamates meteorological datasets with satellite imagery, asserting that this approach significantly enhances the decision-making frameworks pertinent to solar energy initiatives. Additionally, Nawab et al. (2023) juxtaposed empirical methodologies against artificial intelligence-driven strategies, underscoring the critical nature of precise measurement and forecasting in solar radiation assessment. This comprehensive literature review elucidates the efficacy of artificial neural networks in the context of global solar radiation prediction and advocates for the viability of ANN-centric modeling within regions endowed with high solar energy potential, such as Mersin province. The accumulated findings delineate the preeminence of ANN in elucidating nonlinear associations and propose an avant-garde approach to solar radiation forecasting. Collectively, these investigations illustrate that the ANN frameworks tailored for Mersin province are poised to yield substantial advancements in both regional energy policies and the broader scientific discourse.

Through the comprehensive analyses undertaken at the regional level, this study endeavors to elucidate the merits of artificial neural networks in the prediction of global solar radiation, thus positioning itself as a pioneering contribution to the existing body of literature in this domain. The overarching framework of the investigation is comprised of a series of interrelated segments, which encompass an introductory discourse on the subject matter, foundational theoretical insights pertaining to solar radiation and the operational principles of artificial neural networks, a meticulous literature review, a detailed exposition of the research methodology employed, a thorough data analysis accompanied by resultant findings, and ultimately, a synthesis of conclusions alongside actionable recommendations. The insights garnered from this work are poised to enrich the ongoing dialogue surrounding the integration of advanced predictive models in solar radiation forecasting.

SOLAR RADIATION AND ARTIFICIAL NEURAL NETWORKS (ANNs)

As evidenced by the extensive body of research available, the role of solar radiation within the Earth's energy cycle is undeniably critical, underpinning both natural phenomena and various climatic occurrences. Furthermore, this radiation plays an indispensable role in an array of fields, encompassing climate change, agricultural productivity, energy generation, and broader environmental dynamics. To quantify solar radiation accurately, a variety of instrumentation is employed, including but not limited to pyranometers, pyrheliometers, heliographs, shadow-band pyranometers, and sunshine recorders. The selection of these measurement tools is contingent upon the specific data requirements and the intended application of the gathered information. Such methodological diversity is essential for advancing our understanding of solar energy's multifaceted impacts on both ecological and human systems (Sengupta et al., 2021; Kumar et al., 2020; Ahmed et al., 2020).

As illustrated in the extensive reviews conducted, the modeling and forecasting of solar radiation are pivotal in the architecture and functionality of renewable energy frameworks. It has become increasingly evident that dependable prediction methodologies are essential, particularly for the thorough assessment of solar energy systems, radiation budget analyses, and the operational efficacy of photovoltaic installations. Nevertheless, the establishment of such predictive techniques often hinges upon inputs that are prohibitively expensive. In this investigation, a comprehensive examination was undertaken to evaluate various existing prediction models, juxtaposing their performance against real-world data derived from operational solar energy systems. Furthermore, the implications of these predictive inaccuracies on the overall system efficiency, investment viability, and long-term sustainability were meticulously scrutinized. The outcomes of this research are anticipated to furnish valuable insights for scholars and practitioners engaged in the enhancement of solar energy predictability while concurrently addressing the associated economic challenges.

As can be observed from the extensive body of research conducted, the computational frameworks known as artificial neural networks (ANNs) have emerged as pivotal tools, inspired fundamentally by the architecture of biological neural networks. These intricate models encompass an input layer, one or more intermediate hidden layers, and a definitive output layer. Within this configuration, the input layer serves to aggregate the data, while the hidden layers adeptly capture the nonlinear interdependencies that exist between the inputs and the resulting outputs, culminating in the output layer which delivers the ultimate prediction or classification. In recent years, the proliferation of ANNs in various domains can be attributed to their remarkable proficiency in modeling complex and nonlinear relationships, coupled with their inherent ability to adapt seamlessly to evolving datasets. This technique has been effectively harnessed across a myriad of applications, including but not limited to pattern recognition, signal processing, financial forecasting, control systems, optimization, and regression analyses, as evidenced by the works of Goncu et al. (2021), Alizamir et al. (2020), Bozkurt et al. (2022), and Kassem et al. (2021). The ongoing exploration of ANNs continues to yield valuable insights, fostering advancements that resonate across multiple disciplines.

As evidenced by the extensive body of research conducted in the realm of solar radiation forecasting, artificial neural networks (ANNs) have emerged as a prevalent methodology within both environmental and energy sectors. These advanced computational techniques facilitate a more precise prediction of forthcoming solar radiation levels, drawing upon a comprehensive analysis of historical datasets. The modeling of solar radiation through such sophisticated means serves as a pivotal instrument for navigating the complexities of climate change and enhancing the efficacy of renewable energy infrastructures. Furthermore, the utilization of ANNs confers substantial advantages in diverse applications, encompassing the design and performance evaluation of solar energy systems, by providing cost-effective and adaptable solutions that stand in stark contrast to conventional methodologies (Ozturk, 2020). The insights gleaned from this approach are anticipated to significantly contribute to the ongoing discourse surrounding the optimization of renewable energy technologies.

In light of the considerations presented, this investigation meticulously modeled the daily average solar radiation for the Mersin province through the application of artificial neural networks (ANNs), thereby presenting a methodology that transcends conventional techniques. This innovative approach not only enhances the landscape of energy planning but also significantly contributes to the advancement of sustainable energy solutions. The findings derived from this study are expected to serve as a valuable resource for stakeholders engaged in the pursuit of efficient energy management and the promotion of renewable energy initiatives. Such insights are deemed crucial for fostering a deeper understanding of solar energy dynamics in the region.

The Role of Solar Radiation and Measurement Techniques

As evidenced by the extensive body of research conducted, solar radiation emerges as the fundamental energy input from the sun to the Earth, exhibiting significant impacts across various domains, including climatic patterns, agricultural productivity, ecosystem dynamics, and energy generation capabilities. This underscores the paramount importance of precise measurement and thorough analysis of solar radiation, which are indispensable for the effective design of renewable energy systems and the comprehensive assessment of environmental processes. Such insights are crucial for advancing our understanding of the intricate interplay between solar energy and its multifaceted effects on both natural and human systems.

As evidenced by the array of measurement instruments utilized in solar radiation assessment, devices such as pyranometers, pyrheliometers, and sunshine recorders play pivotal roles. Furthermore, the integration of ceilometers and mechanical-electronic sunshine recorders facilitates the measurement of critical parameters including sky cover and atmospheric optical depth. The resultant data garnered from these sophisticated devices is initially acquired in a raw format, subsequently undergoing meticulous time correction methodologies to ensure analytical readiness. Nonetheless, it is imperative to acknowledge that the precision, financial implications, and user-friendliness of these measurement instruments exhibit considerable variability, contingent upon the specific application domain.

As evidenced by the comprehensive analyses undertaken, the utilization of satellite-based solar radiation data stands out as a particularly advantageous alternative, particularly in scenarios where terrestrial measurement stations are conspicuously absent. Such satellite-derived data holds substantial promise for both grid-based solar radiation forecasting and validation endeavors. Nevertheless, it is imperative to acknowledge that inherent quality concerns and measurement inaccuracies associated with satellite data may compromise the reliability of the findings. Consequently, the advancement of predictive models leveraging satellite imagery emerges as a pivotal opportunity for enhancing the precision of solar radiation estimations. Contemporary satellites, in contrast to their predecessors, furnish data characterized by superior spatial and temporal resolution, thus conferring a notable benefit in the realm of solar radiation forecasting (Guijo-Rubio et al., 2020; Narvaez et al., 2021).

As highlighted by the examination of various methodologies in the field, the assessment of solar radiation measurement techniques has demonstrated that the precision in data acquisition is paramount. Furthermore, the contemporary landscape reveals that these techniques are not merely confined to the realm of data collection; rather, they serve as vital instruments in strategic energy production planning and the formulation of early warning systems. In this regard, the synergistic implementation of satellite-based and ground-based measurement approaches emerges as a pivotal strategy, facilitating the optimization of energy generation processes while concurrently advancing the development of sustainable energy solutions. The insights gleaned from this multifaceted approach are expected to significantly influence ongoing research and practical applications in the renewable energy sector.

Artificial Neural Networks

As illustrated through the extensive research conducted on the application of Artificial Neural Networks (ANNs), it is apparent that these sophisticated artificial intelligence systems, which draw inspiration from the intricate architecture of the human brain, possess remarkable capabilities. Specifically, ANNs are adept at discerning patterns within data, thereby enabling them to model complex and nonlinear relationships with notable precision. Their versatility is evidenced by their successful implementation across a myriad of domains, including but not limited to finance, medicine, industry, and agriculture. The inherent flexibility and adaptability of ANNs stem primarily from their robust learning mechanisms, which empower them to extract valuable insights from intricate datasets (Amaratunga et al., 2020; Montesinos et al., 2022). Such findings are anticipated to serve as a significant resource for researchers and practitioners seeking to harness the potential of ANNs in diverse applications.

As evidenced by the extensive body of research conducted, artificial neural networks (ANNs) present a noteworthy advantage in the modeling of climatic behaviors and the forecasting of non-stationary datasets, particularly in the realm of solar radiation. The implementation of multi-layer ANNs in the prediction of solar radiation has garnered success across various domains, encompassing energy production forecasting, photovoltaic system applications, the operational performance of solar thermal collectors, as well as the prediction of both global and diffuse solar radiation. Such methodologies provide a formidable instrument for addressing complex phenomena while elucidating the intrinsic characteristics of data (Geetha et al., 2022; Mukhtar et al., 2022; Guo et al., 2024). The expansive applicability of ANNs underscores their burgeoning potential within solar radiation research, thereby playing a pivotal role in the quest for solutions to the pressing energy challenges of our time.

In light of the advancements in computational methodologies, the utilization of artificial neural networks for solar radiation modeling has emerged as a markedly superior alternative to traditional statistical techniques. Their inherent capacity to discern non-linear dependencies and evaluate intricate frameworks enables the attainment of exceptional precision in forecasts pertaining to solar radiation. Consequently, this phenomenon positions artificial neural networks as an invaluable asset in the realm of solar radiation prediction, as evidenced by contemporary studies (Chiu et al., 2022; Movassagh et al., 2023). Through this lens, it becomes evident that the integration of such sophisticated modeling tools can significantly enhance the reliability and accuracy of solar energy assessments.

The characteristics that set artificial neural networks apart from traditional methodologies are manifold: their capacity to model intricate nonlinear relationships, their independence from specific distributional assumptions, and their lack of a requisite predetermined input structure. Furthermore, they exhibit resilience against noise and the complexities inherent in variable interactions, allowing for adaptability to fluctuating meteorological conditions with minimal restrictions. As data accumulates, they possess the remarkable ability to enhance their performance, adeptly unraveling a multitude of relationships and variations. This inherent flexibility in managing extensive datasets underpins their significance (Movassagh et al., 2023; Markidis, 2021). Such advantages position artificial neural networks as indispensable instruments for solar radiation forecasting, particularly within regions endowed with substantial solar energy potential, exemplified by the Mersin province. Their distinctive capabilities lay a robust groundwork for energy planning and the formulation of sustainable energy strategies. By capitalizing on their versatility and precision, ANN-driven methodologies propel the domain of solar radiation prediction forward, rendering a meaningful contribution to both the scientific sphere and practical implementations, especially in areas abundant in solar resources.

METODOLOGY

To accurately model the long-term global solar radiation in the Mersin province, this investigation employed Artificial Neural Networks (ANNs), adhering to a meticulously structured methodology that encompassed several critical steps. Initially, a comprehensive dataset was compiled, capturing various atmospheric parameters relevant to solar radiation patterns. Subsequently, the data underwent rigorous preprocessing to ensure its integrity and suitability for the ANN framework. Following this, an optimal ANN architecture was designed, taking into consideration the intricacies of the data and the specific objectives of the study. The training phase involved the application of advanced algorithms to refine the model's predictive capabilities. Furthermore, validation processes were implemented to assess the reliability and accuracy of the ANN outputs against established benchmarks. Ultimately, the findings of this research are anticipated to contribute significantly to the field of solar energy, offering valuable insights for future applications and studies focusing on solar radiation modeling in similar climatic regions.

Data Collection and Preprocessing

The investigation embarked upon a meticulous examination of a voluminous dataset accumulated over a decade, encapsulating measurements of solar radiation. Within the context of the modeling framework, the pivotal input variables were delineated as solar altitude angle, wind speed, and dry-bulb temperature, with the direct solar radiation value designated as the output variable of interest. In the initial phase of data preprocessing, the challenge of missing values was adeptly tackled through the application of interpolation techniques, thereby bolstering the integrity of the dataset. Subsequently, the dataset underwent normalization to align with the stringent input prerequisites of the model, a process that not only ensured uniformity but also significantly enhanced computational efficacy. The insights gleaned from this meticulous approach are anticipated to contribute substantially to the ongoing discourse in the field of solar energy modeling.

Design of the Artificial Neural Network Model

The artificial neural network (ANN) model was meticulously developed employing MATLAB’s Neural Fitting Tool (nfttool), encompassing a tri-layer architecture: an input layer, a solitary hidden layer, and an output layer. The hidden layer was meticulously configured with 30 neurons, a decision made to strike an optimal equilibrium between the complexity of the model and computational efficacy. During the training phase, the Levenberg-Marquardt backpropagation algorithm was judiciously implemented, recognized for its rapid convergence and proficiency in managing datasets of moderate scale. Furthermore, this methodological choice is anticipated to yield robust predictive capabilities, thereby facilitating enhanced understanding of the underlying patterns within the data. The outcomes derived from this study are expected to contribute significantly to the ongoing discourse in the realm of neural network applications.

As illustrated in Figure 1, a comprehensive schematic diagram delineates the intricate integration of input and output variables within the architecture of the artificial neural network (ANN), alongside the systematic organization of the dataset. This meticulous configuration is paramount, as it underpins the precise execution of the learning process, thereby facilitating optimal performance and reliability in the ensuing analyses. Such arrangement not only enhances the functional capabilities of the ANN but also ensures that the derived outcomes are both valid and replicable, thus contributing to the overarching goals of the research endeavor.

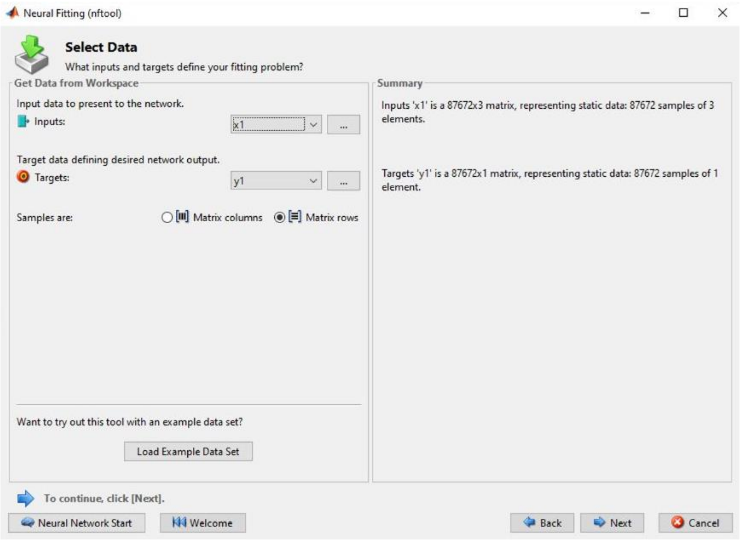

Figure 1: Definition of Input and Output Data Structure for Artificial Neural Network

In the configuration presented, the input dataset, identified as x_1, is meticulously arranged into a matrix comprising 87,672 samples distributed across three distinct variables. Correspondingly, the output dataset, symbolized as y_1, is constructed as a matrix that likewise contains 87,672 samples aligned with a singular variable. This systematic organization facilitates the artificial neural network's capacity to adeptly discern and encapsulate the intricate interdependencies that exist between the input and output variables, thereby enhancing the overall modeling efficacy.

It is evident from the detailed analysis conducted on the input-output datasets that the meticulous structuring significantly enhances the model's training efficacy, leading to a notable increase in predictive precision. Moreover, this sophisticated modeling architecture facilitates the forecasting of long-term global solar radiation, thereby offering a reliable instrument for strategic initiatives, including energy resource planning and the optimization of renewable energy infrastructures. Furthermore, the implications of such advancements are anticipated to resonate throughout various sectors, ultimately contributing to a more sustainable energy landscape. The findings presented here are poised to serve as a valuable reference for practitioners and researchers dedicated to the advancement of renewable energy technologies.

The Artificial Neural Network (ANN) architecture is meticulously designed with three integral layers: an input layer, a singular hidden layer, and an output layer. The input layer is constituted of three distinct neurons, each directly aligned with one of the critical input variables—solar altitude angle, wind speed, and dry-bulb temperature. In contrast, the hidden layer is endowed with 30 neurons, judiciously arranged to facilitate the acquisition of complex, non-linear correlations while adeptly capturing the subtle interdependencies that exist between the input and output variables. The output layer is comprised of a solitary neuron, which serves to encapsulate the predicted value of direct solar radiation. This structured approach is anticipated to yield insights into the multifaceted dynamics governing solar energy interactions.

As illustrated in Figure 2, a comprehensive schematic representation of the model's architecture is presented. It is evident that the artificial neural network (ANN) model initiates with three input neurons, subsequently advancing through a hidden layer comprising 30 neurons, and culminating in a solitary neuron within the output layer. The hidden layer functions as the computational nucleus, utilizing its 30 neurons to effectively capture intricate, non-linear relationships inherent within the dataset. This specific arrangement of the hidden layer was meticulously selected to optimize training efficiency while concurrently achieving elevated predictive accuracy.

The architectural configuration delineated herein effectively harmonizes computational efficiency with the learning aptitude of the model, thereby enabling the Artificial Neural Network (ANN) to attain a commendable degree of precision in the forecasting of solar radiation. Furthermore, the model has been robustly employed in the prediction of solar radiation within the Mersin province, underscoring its utility in facilitating energy planning and enhancing the optimization of renewable energy systems. In light of the aforementioned, the implications of this work are anticipated to furnish invaluable insights for researchers and practitioners dedicated to advancing the integration of renewable energy sources.

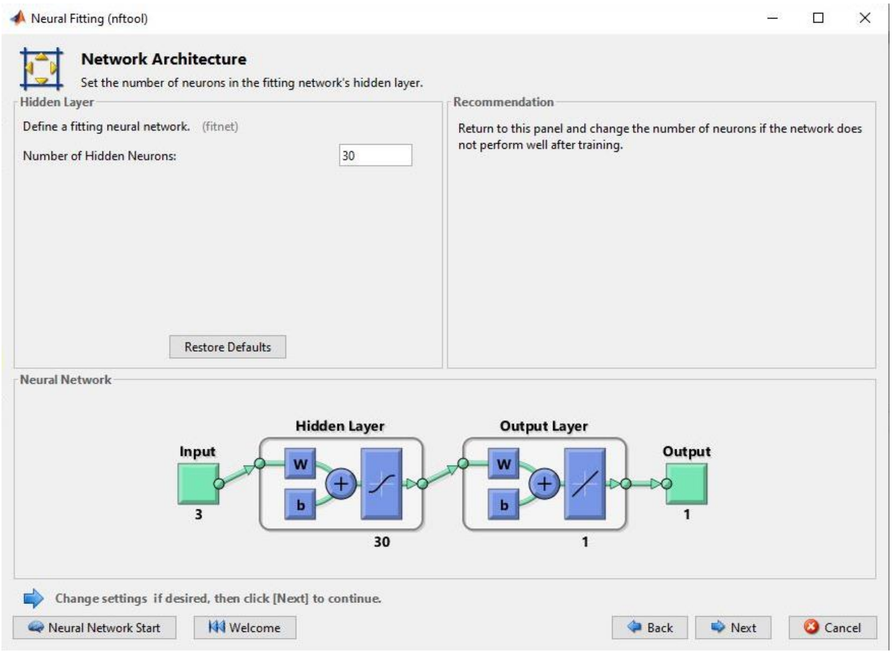

Figure 2: Artificial Neural Network Architecture and Layer Structure

Data Partitioning and Model Training

In the domain of Artificial Neural Network (ANN) modeling, the segmentation of the dataset into training, validation, and testing subsets emerges as an indispensable procedure for appraising the model's efficacy and ensuring its capacity to generalize effectively. Within the framework of this investigation, the dataset, comprising a substantial total of 87,672 samples, was judiciously randomized into three distinct subsets to facilitate the modeling endeavor. The training subset, encompassing 75% of the overall data, was engaged to cultivate the ANN model, enabling it to discern intricate patterns and interrelationships inherent within the dataset. Concurrently, the validation subset, which constituted 15% of the data, was employed to vigilantly track the model's performance throughout the training phase, offering vital insights that contributed to the refinement of the model and the mitigation of overfitting risks. The final 10% of the data was designated to the testing subset, which performed a critical role in the independent evaluation of the model's performance in scenarios reflective of real-world applications.

In examining the methodologies employed in data partitioning, it becomes evident that this systematic framework facilitates a thorough assessment of the model's learning, generalization, and predictive competencies. Furthermore, this approach serves as a robust basis for precise solar radiation forecasting, underscoring the dependability of the artificial neural network (ANN) model in real-world scenarios. By emphasizing these aspects, the study aims to contribute valuable insights for those engaged in the advancement of forecasting techniques.

As illustrated in the accompanying Figure 3, the comprehensive dataset, consisting of 87,672 distinct samples, was meticulously partitioned into three specific subsets: a dominant 75% designated for training (65,754 samples), a critical 15% allocated for validation (13,151 samples), and a final 10% reserved for testing (8,767 samples). The training subset served as the foundation for the learning trajectory of the Artificial Neural Network (ANN) model, focusing on the reduction of prediction errors and the meticulous adjustment of model parameters. The validation subset assumed a crucial function in evaluating the model's capacity for generalization and in mitigating the risks of overfitting throughout the training phase. In parallel, the testing subset, intentionally set aside for independent assessment, was utilized to gauge the model's predictive accuracy on data that had not been previously encountered. This tripartite division strategy establishes a solid framework for enhancing the precision of the ANN model, thereby ensuring dependable predictions in the intricate domain of solar radiation forecasting.

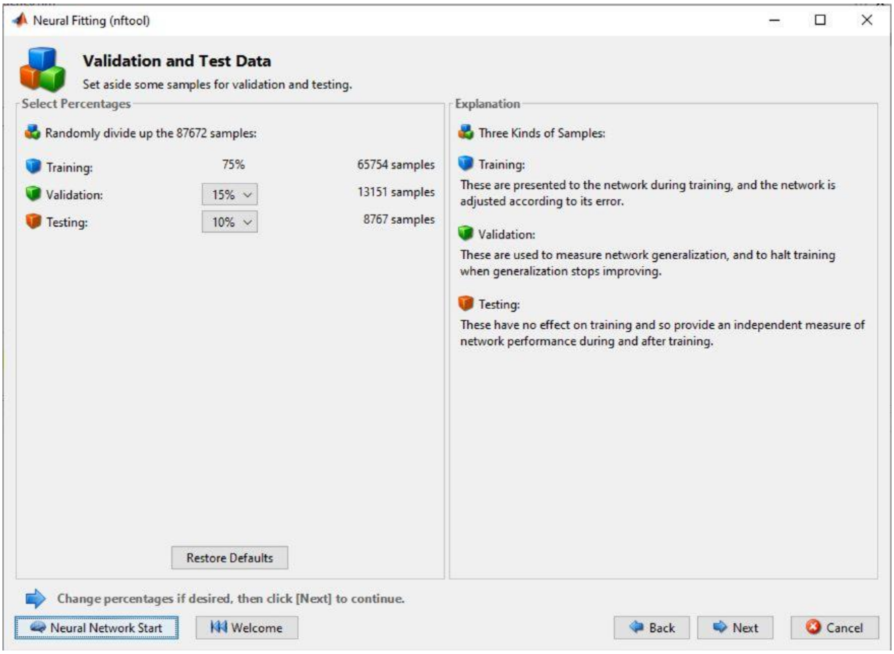

Figure 3: Percentage Distribution of the Dataset for Training, Validation, and Testing

The meticulous partitioning of the dataset into training, validation, and testing subsets exemplifies a refined strategy aimed at optimizing model efficacy. The training subset served as the foundational support for the learning framework, while the validation subset played a critical role in assessing the model’s capacity to generalize across diverse scenarios. Conversely, the testing subset was reserved exclusively to appraise the model’s predictive performance in conditions that closely mirror real-world applications. To ensure a streamlined and precise training process, the Levenberg-Marquardt algorithm was employed, revered for its rapid convergence and commendable accuracy, making it exceptionally appropriate for datasets of moderate dimensionality. Additionally, a robust automated termination protocol was integrated, which ceased the training when an escalation in validation set error became apparent, thus further fortifying the model’s ability to generalize effectively.

As evidenced by the comprehensive evaluation conducted across the three distinct subsets—training, validation, and testing—the performance of the ANN model has been scrutinized to ascertain its robustness and reliability. Furthermore, Figure 4 presents a visual representation of the intricate training process, effectively illustrating the results alongside the performance metrics. This depiction underscores the model's remarkable proficiency in predicting solar radiation with a level of accuracy that is indeed noteworthy. Such findings are anticipated to serve as a valuable resource for researchers delving into advancements in predictive modeling within the field.

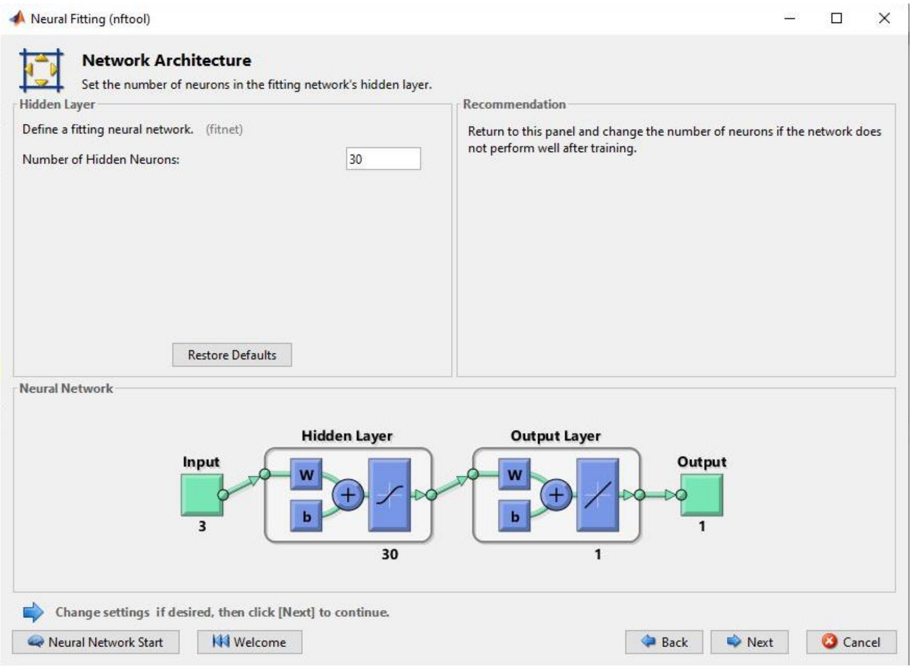

Figure 4: Artificial Neural Network Training Process and Performance Evaluation Results

As evidenced by the detailed statistical analysis conducted, the model in question was subjected to a rigorous evaluation process, employing a total of 65,754 samples designated for training, alongside 13,151 samples allocated for validation, and 8,767 samples reserved for testing purposes. The resulting Mean Squared Error (MSE) values were computed as 9.034×10^{-4} for the training dataset, 9.488×10^{-4} for the validation dataset, and 8.434×10^{-4} for the testing dataset, reflecting the model's predictive performance. Furthermore, the regression coefficient (R) values consistently surpassed the threshold of 0.90 across all utilized datasets—training, validation, and testing—serving as a testament to the model's remarkable accuracy and its robust capacity for generalization across varied data conditions. The implications of these findings are anticipated to significantly contribute to the ongoing discourse among researchers focused on the enhancement of predictive modeling methodologies.

The findings presented herein elucidate the remarkable efficacy of the artificial neural network (ANN) model in discerning and delineating intricate patterns and interrelationships embedded within the dataset. In light of this, the results serve to confirm the model's dependability and resilience as a mechanism for forecasting solar radiation. Its evidenced precision and capacity for generalization position it as a highly promising methodology for tangible applications, including energy strategizing and the enhancement of renewable energy frameworks.

RESULTS and DISCUSSIONS

In examining the extensive outcomes derived from the long-term forecasting of global solar radiation utilizing the Artificial Neural Network (ANN) model, it becomes evident that a comprehensive analysis is warranted. The figures presented herein afford profound insights into the model's performance throughout the critical phases of training, validation, and testing, thereby underscoring its adeptness in discerning intricate patterns and producing precise predictions. Such visual depictions serve to elucidate the robustness and dependability of the ANN model, affirming its efficacy in the realm of solar radiation forecasting. This exploration is anticipated to be of substantial value to researchers engaged in advancing predictive methodologies in solar energy applications.

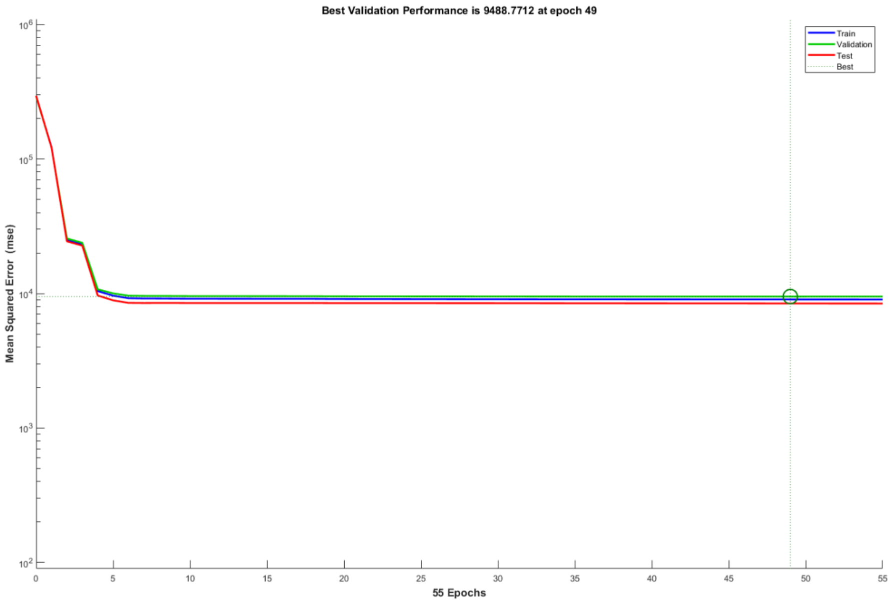

Figure 5: Training, Validation, and Test Performance (Error Analysis)

As illustrated in Figure 5, the Mean Squared Error (MSE) values derived from the diverse phases of training, validation, and testing of the Artificial Neural Network (ANN) model reveal a noteworthy trend. It is evident that the error rates exhibited a steady decline with each iteration throughout the training process, culminating in optimal validation performance by epoch 49. The graphical depiction accentuates a parallel progression between validation and test errors in relation to the training errors, underscoring the model's robust capacity for generalization. Crucially, the consistent absence of any escalation in validation error during the course of training serves as a compelling indication that the phenomenon of overfitting was adeptly mitigated.

As evidenced by the comprehensive analysis undertaken, the advancements in ANN-based modeling for long-term solar radiation forecasting have underscored its superiority relative to conventional methodologies. Furthermore, the findings illuminate the remarkable efficiency of the Levenberg-Marquardt algorithm, which facilitated swift convergence while simultaneously amplifying model precision. This further substantiates the ANN’s adeptness at managing intricate predictive challenges with an impressive degree of reliability. The implications of these results are poised to significantly enrich the discourse surrounding predictive modeling in renewable energy applications, offering a valuable resource for scholars and practitioners alike.

These results confirm that the modeling performed with artificial neural networks is superior to traditional methods and demonstrate the success of the Levenberg-Marquardt algorithm in providing fast convergence and accuracy.

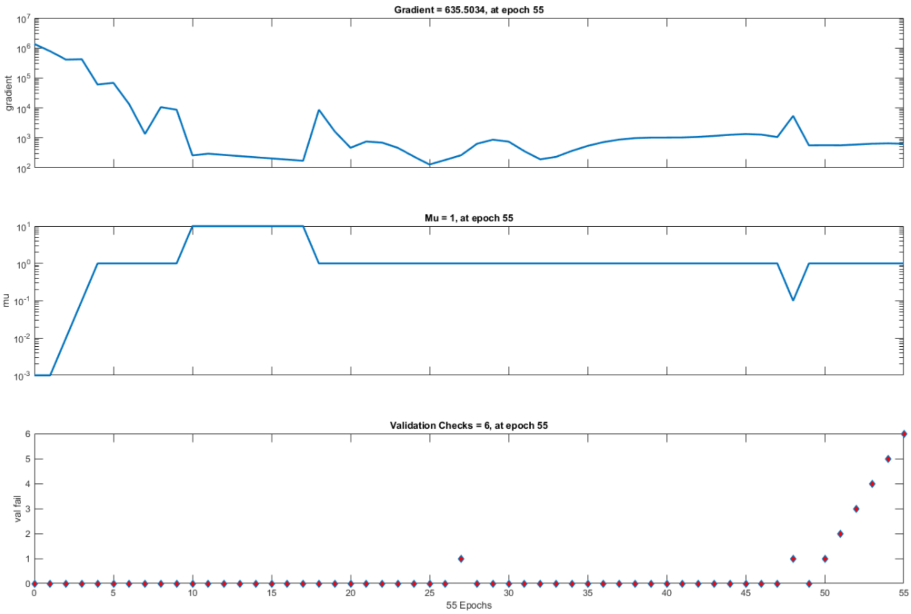

Figure 6: Error Trends and the Influence of Variables

As illustrated in Figure 6 examined, the performance metrics of the artificial neural network (ANN) model have been meticulously analyzed, with particular emphasis on gradient values, the learning rate (μ), and the validation checks conducted throughout the process. The initial graph distinctly reveals a significant decrease in gradient values as the iterations progress, underscoring the model's adeptness at effectively minimizing errors. This persistent reduction emphasizes the model's proficiency in adjusting its parameters with precision, ultimately attaining a state of optimal performance. Furthermore, the subsequent visual data corroborate the robustness of the learning rate, highlighting its pivotal role in facilitating the convergence of the model during the training phase. Such insights are anticipated to serve as valuable contributions to the body of knowledge for researchers focused on enhancing the efficacy of ANN applications in complex data environments.

The subsequent illustration delineates the error distribution (σ), indicative of the model's fidelity to a meticulously structured error minimization pathway. Such a deliberate approach mitigated the risks of excessive fine-tuning, thereby ensuring consistency during the validation period. The unwavering nature of the error distribution further accentuates the reliability of the Adam optimization method in harmonizing swift convergence with accuracy.

As illustrated by the comprehensive validation checks conducted, the graphical representation substantiates the model's efficacy in addressing overfitting throughout the validation phase. The observed low values during these validation checks correspond directly with the steady decline in gradient, thereby fortifying the model's ability to generalize with notable effectiveness. Furthermore, this alignment between validation metrics and gradient behavior serves to enhance the confidence in the model's predictive performance across diverse datasets. Such findings are anticipated to offer valuable insights for practitioners and researchers engaged in modeling endeavors, particularly in the realm of ensuring robust and reliable outcomes.

In light of the comprehensive analysis presented, the consistent decline in gradient, coupled with the stable learning rate and the negligible values observed during validation checks, indicates a proficient execution of the error minimization algorithm alongside a seamless learning trajectory. Furthermore, these observations substantiate the model's adept adjustment to both training and validation datasets, ultimately resulting in a dependable and high-performing output for solar radiation forecasting. This meticulous approach underscores the significance of optimizing learning mechanisms in the pursuit of enhanced predictive accuracy within complex environmental systems.

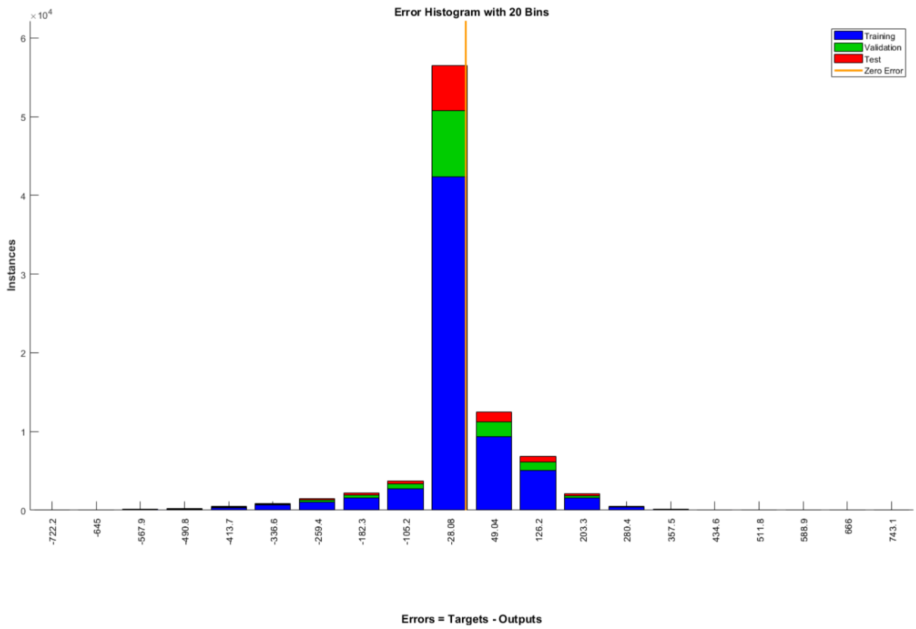

Figure 7: "Error Histogram

In examining the graphical representation provided in Figure 7, one observes the distribution of errors associated with the model's predictions depicted as a histogram. It is evident that a significant proportion of these errors congregate in proximity to the zero mark, underscoring the impressive predictive accuracy inherent in the ANN model and the presence of minimal systematic discrepancies. This pronounced aggregation of errors around the zero threshold serves to illustrate the model's adeptness at producing outputs that closely align with the corresponding actual values, thereby affirming its efficacy in predictive analytics.

As evidenced by the comprehensive analysis conducted on the performance metrics of the model across various datasets, the uniformity observed in error distributions among the training, validation, and testing phases distinctly underscores the robust generalization capabilities of the model. Moreover, the pronounced concentration of errors in proximity to the zero mark serves to bolster the assertions regarding the model's reliability and accuracy in predicting solar radiation levels. This consistency is anticipated to offer valuable insights to researchers and practitioners engaged in the optimization of solar energy forecasting methodologies.

As can be observed from the analytical assessments conducted, the low-error concentration identified within the model presents significant implications for practical applications. This underscores not only the robustness of the model but also its suitability for pivotal undertakings, including energy planning and the optimization of renewable energy systems. Furthermore, these findings substantiate the potential of the ANN model in contexts where high accuracy and reliability are of paramount importance, thereby highlighting its relevance in advancing the field.

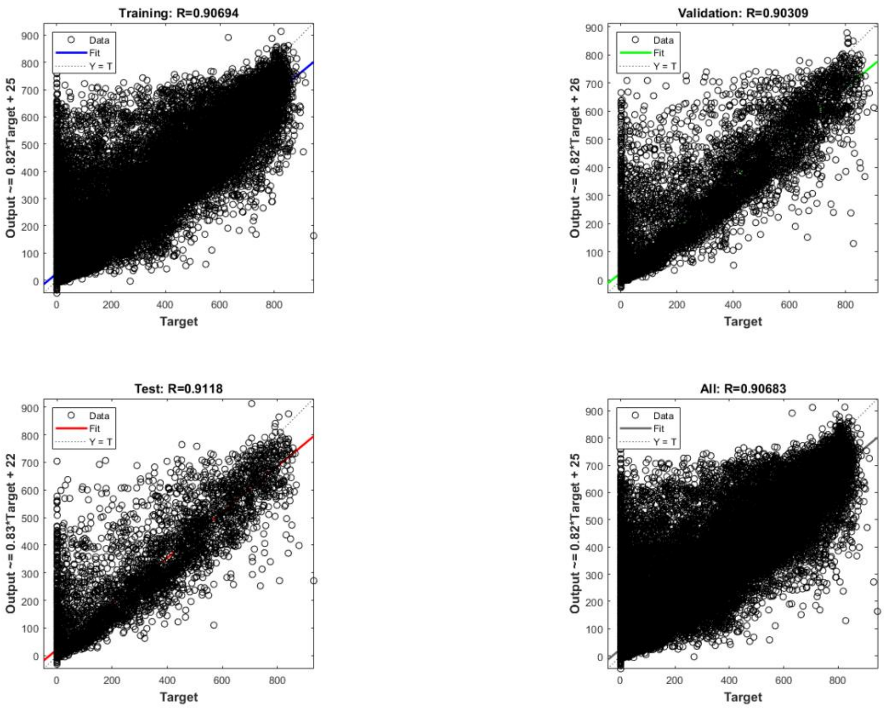

Figure 8: Regression Analysis

As illustrated in the comprehensive analysis of the regression findings presented in Figure 8, the results obtained from the training, validation, and testing datasets of the model reveal a compelling narrative. The coefficients of determination (R) were meticulously computed, resulting in values of 0.90694 for the training dataset, 0.90309 for the validation dataset, and 0.91118 for the testing dataset. Such persistently elevated R values, all exceeding the commendable threshold of 0.90, underscore the model's competence in adeptly elucidating the intricate non-linear associations between the input variables and the target variable. Additionally, the consolidated R value of 0.90683 spanning the entirety of the dataset further substantiates the model’s robustness and its predictive prowess, solidifying its standing as a reliable tool for analysis.

The analysis conducted herein elucidates a significant correlation existing between the projected and observed values, thereby underscoring the model's inherent precision and resilience. Such revelations accentuate the model's versatility across diverse datasets, rendering it applicable to an array of scenarios, particularly in the realm of solar radiation prediction. This investigation, which aspires to construct an ANN-based framework for the long-term forecasting of global solar radiation specifically within the Mersin province, employed an extensive dataset spanning a decade of meteorological observations. By integrating key variables such as solar altitude angle, wind velocity, and dry-bulb temperature, the model adeptly capitalized on the advantageous attributes intrinsic to ANNs, notably their capacity for generalization and exceptional accuracy.

The model architecture, as delineated in the preceding analysis, was conceived through the utilization of MATLAB's Neural Fitting Tool (nfttool), subsequently undergoing a meticulous refinement process informed by a methodical data partitioning strategy—allocating 75% of the dataset for training, 15% for validation, and the remaining 10% for testing purposes. A strategic deployment of 30 neurons within the hidden layer, in conjunction with the implementation of the Levenberg-Marquardt algorithm, facilitated a swift convergence while effectively minimizing errors. The empirical findings underscore a commendable performance, highlighted by elevated R values across all evaluative phases and notably low Mean Squared Error (MSE) metrics, thereby substantiating the model's adeptness in generalizing and yielding dependable predictive outcomes.

As evidenced by the comprehensive analyses conducted, the significance of precise solar radiation forecasting in the realm of renewable energy planning and photovoltaic system design cannot be overstated. Recent advancements have led to the development of an artificial neural network (ANN) model, which, as highlighted in this study, presents a robust and remarkably accurate alternative to traditional forecasting methodologies. This innovative approach not only underscores the potential for optimizing energy production but also illustrates its capacity to significantly improve the efficient utilization of renewable energy resources. Furthermore, the implications of this model are poised to greatly assist in the successful implementation of various energy projects, thereby contributing substantially to the advancement of sustainable energy solutions.

REFERENCES

Ahmadi, M. H., Baghban, A., Sadeghzadeh, M., Zamen, M., Mosavi, A., Shamshirband, S., ... & Mohammadi-Khanaposhtani, M. (2020). Evaluation of electrical efficiency of photovoltaic thermal solar collector. Engineering Applications of Computational Fluid Mechanics, 14(1), 545-565.

Ahmed, R., Sreeram, V., Mishra, Y., & Arif, M. D. (2020). A review and evaluation of the state-of-the-art in PV solar power forecasting: Techniques and optimization. Renewable and Sustainable Energy Reviews, 124, 109792.

Alizamir, M., Kim, S., Kisi, O., & Zounemat-Kermani, M. (2020). A comparative study of several machine learning based non-linear regression methods in

estimating solar radiation: Case studies of the USA and Turkey regions. Energy, 197, 117239.
Amaratunga, V., Wickramasinghe, L., Perera, A., Jayasinghe, J., & Rathnayake, U. (2020). Artificial neural network to estimate the paddy yield prediction using climatic data. Mathematical Problems in Engineering, 2020(1), 8627824.
Bonanno, F., Capizzi, G., Graditi, G., Napoli, C., & Tina, G. M. (2012). A radial basis function neural network based approach for the electrical characteristics estimation of a photovoltaic module. Applied Energy, 97, 956-961.
Bozkurt, H., Macit, R., Çelik, Ö., & Teke, A. (2022). Evaluation of artificial neural network methods to forecast short-term solar power generation: a case study in Eastern Mediterranean Region. Turkish Journal of Electrical Engineering and Computer Sciences, 30(6), 2013-2030.
Chiu, P. H., Wong, J. C., Ooi, C., Dao, M. H., & Ong, Y. S. (2022). CAN-PINN: A fast physics-informed neural network based on coupled-automatic–numerical differentiation method. Computer Methods in Applied Mechanics and Engineering, 395, 114909.
Feng, Y., Hao, W., Li, H., Cui, N., Gong, D., & Gao, L. (2020). Machine learning models to quantify and map daily global solar radiation and photovoltaic power. Renewable and Sustainable Energy Reviews, 118, 109393.
Gao, B., Huang, X., Shi, J., Tai, Y., & Zhang, J. (2020). Hourly forecasting of solar irradiance based on CEEMDAN and multi-strategy CNN-LSTM neural networks. Renewable Energy, 162, 1665-1683.
Geetha, A., Santhakumar, J., Sundaram, K. M., Usha, S., Thentral, T. T., Boopathi, C. S., ... & Sathyamurthy, R. (2022). Prediction of hourly solar radiation in Tamil Nadu using ANN model with different learning algorithms. Energy Reports, 8, 664-671.
Ghazvinian, H., Mousavi, S. F., Karami, H., Farzin, S., Ehteram, M., Hossain, M. S., ... & El-Shafie, A. (2019). Integrated support vector regression and an improved particle swarm optimization-based model for solar radiation prediction. PLoS One, 14(5), e0217634.
Goncu, O., Koroglu, T., & Ozdıl, N. F. (2021). Estimation of hourly global solar radiation using artificial neural network in Adana province, Turkey. Journal of Thermal Engineering, 7(Supp 14), 2017-2030.
Guijo-Rubio, D., Durán-Rosal, A. M., Gutiérrez, P. A., Gómez-Orellana, A. M., Casanova-Mateo, C., Sanz-Justo, J., ... & Hervás-Martínez, C. (2020). Evolutionary artificial neural networks for accurate solar radiation prediction. Energy, 210, 118374.
Guijo-Rubio, D., Durán-Rosal, A. M., Gutiérrez, P. A., Gómez-Orellana, A. M., Casanova-Mateo, C., Sanz-Justo, J., ... & Hervás-Martínez, C. (2020). Evolutionary artificial neural networks for accurate solar radiation prediction. Energy, 210, 118374.
Guo, Q., He, Z., & Wang, Z. (2024). Monthly climate prediction using deep convolutional neural network and long short-term memory. Scientific Reports, 14(1), 17748.
Hoyos-Gómez, L. S., Ruiz-Muñoz, J. F., & Ruiz-Mendoza, B. J. (2021). Short-term forecasting of global solar irradiance with incomplete data. arXiv preprint arXiv:2106.06868.

Kassem, Y., Gökçekuş, H., Çamur, H., & Esenel, E. (2021). Application of artificial neural network, multiple linear regression, and response surface regression models in the estimation of monthly rainfall in Northern Cyprus. Desalination and Water Treatment, 215, 328-346.

Kumar, D. S., Yagli, G. M., Kashyap, M., & Srinivasan, D. (2020). Solar irradiance resource and forecasting: a comprehensive review. IET Renewable Power Generation, 14(10), 1641-1656.

Lauret, P., Rodler, A., Muselli, M., David, M., Diagne, H., & Voyant, C. (2012). A Bayesian model committee approach to forecasting global solar radiation. arXiv preprint arXiv:1203.5446.

Markidis, S. (2021). The old and the new: Can physics-informed deep-learning replace traditional linear solvers?. Frontiers in big Data, 4, 669097.

Martí, P., & Gasque, M. (2011). Improvement of temperature-based ANN models for solar radiation estimation through exogenous data assistance. Energy Conversion and Management, 52(2), 990-1003.

Montesinos López, O. A., Montesinos López, A., & Crossa, J. (2022). Fundamentals of artificial neural networks and deep learning. In Multivariate statistical machine learning methods for genomic prediction (pp. 379-425). Cham: Springer International Publishing.

Movassagh, A. A., Alzubi, J. A., Gheisari, M., Rahimi, M., Mohan, S., Abbasi, A. A., & Nabipour, N. (2023). Artificial neural networks training algorithm integrating invasive weed optimization with differential evolutionary model. Journal of Ambient Intelligence and Humanized Computing, 1-9.

Mukhtar, M., Oluwasanmi, A., Yimen, N., Qinxiu, Z., Ukwuoma, C. C., Ezurike, B., & Bamisile, O. (2022). Development and comparison of two novel hybrid neural network models for hourly solar radiation prediction. Applied Sciences, 12(3), 1435.

Narvaez, G., Giraldo, L. F., Bressan, M., & Pantoja, A. (2021). Machine learning for site-adaptation and solar radiation forecasting. Renewable Energy, 167, 333-342.

Nawab, F., Abd Hamid, A. S., Ibrahim, A., Sopian, K., Fazlizan, A., & Fauzan, M. F. (2023). Solar irradiation prediction using empirical and artificial intelligence methods: A comparative review. Heliyon, 9(6).

Öztürk, C. (2020). Güneş enerji sistemlerinde verim analizi ve enerji kayıplarının tespiti (Master's thesis, Hasan Kalyoncu Üniversitesi).

Palacios, L. E. O., Guerrero, V. B., & Ordoñez, H. (2022). Machine learning model to predict solar radiation, based on the integration of meteorological data and data obtained from satellite images. arXiv preprint arXiv:2204.04313.

Sengupta, M., Habte, A., Wilbert, S., Gueymard, C., & Remund, J. (2021). Best practices handbook for the collection and use of solar resource data for solar energy applications (No. NREL/TP-5D00-77635). National Renewable Energy Lab.(NREL), Golden, CO (United States).

Voyant, C., Muselli, M., Paoli, C., Nivet, M. L., & Poggi, P. (2009). Predictability of PV power grid performance on insular sites without weather stations: use of artificial neural networks. arXiv preprint arXiv:0905.3569.

Yadav, R. K., & Sethy, N. (2018). Solar irradiance prediction using neural model. International Journal of Engineering and Management Research (IJEMR), 8(3), 241-245.

Design and Simulation of a Hybrid Solar-Wind Energy Building for Mersin Province

Fatih ÜNAL[1]
Merve Şentürk ACAR[2]
Bünyamin DEMİR[3]

1- Assoc. Prof. Dr.; Mersin University, Engineering Faculty, Department of Mechanical Engineering. fatihunal@mersin.edu.tr ORCID No: 0000-0001-6660-9984
2- Assoc. Prof. Dr.; Bilecik Şeyh Edebali University, Engineering Faculty, Department of Mechanical Engineering. merve.senturkacar@bilecik.edu.tr ORCID No: 0000-0003-1442-4560
3- Assoc. Prof. Dr.; Mersin University, Engineering Faculty, Department of Mechanical Engineering. bd@mersin.edu.tr ORCID No: 0000-0002-6405-4724

ABSTRACT

In this study, a hybrid solar-wind energy building design model integrated with renewable energy sources was developed for Mersin Province, taking into account the local climatic conditions. The project incorporates 30 photovoltaic panels and a single wind turbine for energy generation. The combined system of solar panels and wind turbines has an annual total energy production capacity of approximately 35,000 kWh. The system is designed for energy storage and an uninterrupted power supply. Mersin's Mediterranean climate, characterized by ample sunshine duration, enhances the efficiency of the solar energy system, while the contribution of wind turbines was evaluated in coastal areas. Simulation studies were conducted using EnergyPlus software, and the performance of the system components was analyzed in detail. The simulation results indicate that the system reduces carbon emissions by approximately 20 tons annually and has a short payback period of 7 years. The study demonstrates that hybrid systems are a significant solution in terms of energy efficiency and sustainability. The proposed design meets the energy demand while reducing dependence on the grid and providing economic savings. This project is an example of future hybrid energy buildings and demonstrates the potential for more effective use of renewable energy sources in building design.

Keywords – Hybrid Energy System, Renewable Energy, Photovoltaic Panel, Wind Turbine, Energy Efficiency.

INTRODUCTION

This study introduces a model for a hybrid solar-wind energy building designed for Mersin Province, integrating renewable energy sources while considering local climatic conditions. This model aims to enhance energy efficiency and reduce energy costs. Furthermore, the integration of hybrid systems will enable building occupants to benefit maximally from sustainable energy. The primary objective of this research is to underscore the significance of hybrid energy building design in terms of sustainability, energy efficiency, and environmental impact. In this context, the integration of innovative technologies in the design processes of hybrid energy buildings is intended to reduce energy consumption. In this process, the combined use of solar energy systems, wind energy solutions, and energy storage systems gains importance.

The literature on the design and simulation of hybrid energy buildings is increasingly growing. In this regard, various methods and techniques are being developed to improve energy efficiency. The integration of hybrid solar-wind energy systems into building designs has garnered increasing attention in recent years due to the need for sustainable and efficient energy solutions. This literature review contributes to the understanding of hybrid systems by addressing various studies on their design, simulation, and application for buildings and remote areas for energy generation purposes.

Gadkari (2008) presents a pioneering study on a reconfigurable hybrid solar and wind energy system that focuses on the feasibility of infrastructure sharing between solar and wind components. The research highlights the innovative use of parabolic concentrators for both solar energy collection and wind energy conversion, indicating that such hybrid systems could be suitable alternatives in regions with low energy demand.

Abreu et al. (2011) delve deeper into the discussion of hybrid energy systems by exploring the benefits of passive systems based on air movement in buildings. Their study shows that the integration of wind turbines into building designs can enhance indoor comfort while generating electricity. The authors advocate for the architectural integration of solar and natural airflow systems, which could enhance energy efficiency and economic feasibility.

Bakić et al. (2012) studied photovoltaic/wind systems that include hydrogen storage, stating that hybrid systems can significantly improve efficiency and reliability compared to standalone systems. Their simulation-based study reveals that integrating solar thermal and photovoltaic components can meet the energy needs of residential buildings and increase economic feasibility.

In the same year, Vukman et al. (2012) reiterated the advantages of hybrid power systems, particularly focusing on reducing emissions and supporting grid stability. Their work emphasizes the importance of dynamic simulations in understanding the performance of hybrid systems and provides insights into the operational management of solar PV-wind energy systems.

Schijndel (2016) introduces finite element methods (FEM) for building energy simulation, demonstrating the potential for complex 3D modeling that includes various factors like ventilation and radiation. This approach allows for more detailed assessments of building energy performance to optimize the design of hybrid energy systems.

Nnadi et al. (2017) investigated the application of hybrid solar-wind generation systems for electrification in remote areas. The simulation results indicate that such systems can effectively improve living standards in areas without access to the traditional grid. The study underscores the complementary nature of solar and wind resources, suggesting that hybrid systems can offer reliable energy solutions for rural populations.

Assaf (2018) expands on the integration of solar and hydrogen systems for heat and power applications. Using TRNSYS software for modeling and simulation to understand the energy performance of these systems offers a comprehensive approach. The literature review in the study highlights the growing interest in hydrogen systems, presenting them as a viable energy solution for residential applications.

Vadakkepurakkel (2019) focuses on the design of a hybrid power generation system that combines solar and wind energy to sustainably meet global energy demands. The research highlights the importance of maximum power tracking techniques and control strategies to optimize energy generation from both sources.

Nyemba et al. (2019) conducted a parametric study of hybrid power generation systems, further enhancing the understanding of hybrid energy solutions. Their work emphasizes the importance of spatial assessments and feasibility studies in the context of rural electrification, reinforcing the need for solutions tailored to different geographical conditions.

Bhatti et al. (2022) explore machine learning techniques to accelerate the discovery of high-performance solar panels, highlighting the potential for integrating advanced technologies in renewable energy systems. Their systematic review provides insights into the importance of optimizing solar panel performance to enhance the efficiency of hybrid systems.

Hosseini (2023) presents three-level mathematical models to optimize energy efficiency, storage performance, and greenhouse gas emissions for hybrid renewable energy systems. This model represents a significant advance in the strategic planning of hybrid energy systems, aligning with sustainability and environmental responsibility goals.

The synthesis of these contributions aims to provide a comprehensive understanding of the design and simulation of hybrid solar-wind energy systems. The study highlights the potential applications of these systems in building energy solutions and rural electrification initiatives. Solar energy is a clean and renewable energy source that is increasingly attracting attention from society. The proper utilization of this energy source depends on the optimal design of the systems. To design these systems, the amount of solar radiation on the earth's surface is the most important parameter, and the global model of this radiation can be expressed on an annual, monthly, and daily basis. These models can be made using empirical mathematical models, artificial neural networks, and relationships with air temperature and humidity. However, the results are not very reliable in models developed with air temperature and humidity relationships due to the high nonlinearity of the data. Meteorological and climatic data are needed to estimate global radiation on the Earth's surface. However, in some underdeveloped regions, observations at regular time intervals are not possible due to technical operations and economic costs. These reasons also limit the number of stations in some regions.

Global radiation models developed using empirical models, artificial intelligence approaches, and air temperature and humidity relationships can be divided into two main groups: linear and nonlinear. Mathematical models forming the first group contain trigonometric and exponential functions and are quite well known. Among all global models, the most well-known one is the one presented by Gutzhants. These models are based on the least squares approach used during the model development phase. Numerous examples developed with this approach have provided frequently used coefficients and results. Artificial neural networks, as members of the second group, are widely applied in many scientific studies. The most important reason for these methods is their nonlinear nature. Ease of use and good prediction ability make artificial neural networks one of the most preferred methods (Souza, 2020; Al-Ghussain et al., 2020; Mokhtara et al., 2020; Ridha et al., 2021; Samek et al., 2021).

Unlike studies on hybrid solar-wind energy systems in the literature, this work presents a locally optimized system design by considering the climatic and environmental characteristics of a specific region, such as Mersin province. Simulations performed using solar panels and a wind turbine analyze the system's performance. By adopting a specific approach to local energy needs, the study focuses on balancing energy generation and consumption.

HYBRID ENERGY SYSTEMS

Hybrid energy systems are systems in which different energy sources are integrated and utilized. These systems typically combine renewable energy sources such as solar, wind, and hydroelectric power with conventional energy sources. Hybrid energy systems provide benefits such as ensuring energy independence, generating environmentally friendly energy, and reducing energy costs. They also create a more resilient energy supply system against power outages (Güven & Mete, 2021; Kara et al., 2022; Işık et al., 2023).

The design and simulation of hybrid energy buildings offer innovative approaches to enhance energy efficiency and create sustainable living spaces. This design process is carried out by integrating renewable energy sources and using various simulation techniques to reduce energy consumption. These simulation techniques are optimized for the effective use of solar energy, wind energy, and other renewable resources. Furthermore, various software and modeling tools are also employed to increase energy efficiency in building design. (Savaş et al., 2022; Yıldız, 2024).

The design and simulation of hybrid energy buildings represent an innovative approach aimed at creating comfortable living spaces with sustainable energy solutions. This approach offers an integrated strategy in building design by utilizing innovative engineering solutions and simulation techniques to increase energy efficiency and reduce environmental impacts.

This strategy focuses not only on the integration of energy systems with building design but also on the use of sustainable materials. Hybrid energy systems have the potential to optimize energy consumption by incorporating renewable energy sources as well as conventional energy sources (Mokhtara et al., 2021; Esmaeilishayan et al., 2022).

HYBRID SYSTEM DESIGN

The hybrid energy system designed in this study integrates solar and wind energy resources to sustainably meet the energy demand of a typical residential building in Mersin. The system incorporates photovoltaic (PV) panels, a vertical axis wind turbine (VAWT), lithium-ion batteries for energy storage, and a microcontroller-based Energy Management System (EMS) that intelligently manages energy flow. This integrated approach aims to provide a more reliable and stable energy generation by leveraging the advantages of both renewable energy sources. The system is designed to be grid-connected (on-grid), which means that excess generated energy can be fed into the grid, and energy can be drawn from the grid when needed. This enhances energy supply security while also contributing to the grid infrastructure. The following subsections will examine the system components and design details more elaborately.

Components of the Hybrid System

The foundation of the hybrid energy system is the synergistic integration of solar and wind energy. This integration combines the unique advantages of both sources, providing a more reliable and continuous energy generation (Roy et al., 2022; Hassan et al., 2023).

The solar energy system converts solar radiation directly into electrical energy through Photovoltaic (PV) panels. In this study, 30 PV panels, known for their high efficiency and durability, were employed. The PV panels utilize polycrystalline silicon technology, with a nominal power output of 120 Wp each. They provide effective energy conversion, especially in regions with abundant sunshine, such as Mersin. The technical specifications of the panels include a cell efficiency of approximately 16%, an open-circuit voltage of 17.5 V, and a short-circuit current of 7.0 A. The primary reasons for selecting these panels are their high performance, long lifespan, and resilience to harsh weather conditions.

The wind energy system is supported by a vertical axis wind turbine capable of generating energy even at low wind speeds. The wind turbine used is notable for its compact design, space-saving advantages, and aesthetic harmony. Vertical axis turbines are suitable for use on building rooftops as they are less sensitive to changes in wind direction. The technical specifications of this turbine include a nominal power output of 1 kW, a cutin wind speed of 3 m/s, and a rated wind speed of 12 m/s. This turbine efficiently harnesses the wind potential of Mersin's coastal areas.

Lithium-ion batteries were used in the energy storage system to ensure energy continuity and meet sudden demand fluctuations. Lithium-ion batteries were preferred due to their high energy density, long lifespan, and fast charge/discharge capabilities. These batteries play a critical role in preventing power outages and reducing dependence on the grid by storing excess generated energy. The battery capacity used in the system was determined based on the building's energy consumption profile and the energy production capacity of the hybrid system.

A microcontroller-based system was implemented as the Energy Management System (EMS) to effectively manage the entire system and optimize energy use. This system continuously monitors the energy produced by both the PV panels and the wind turbine, controls the battery state of charge, and optimizes energy flow according to the building's energy needs. The EMS also manages the grid connection, allowing excess energy to be fed into the grid and energy to be drawn from the grid when needed. Advanced control algorithms maximize the system's efficiency and reliability.

Site Selection and Architectural Design

The site selection for the project was determined to ensure maximum energy efficiency and to make the best use of Mersin's unique environmental conditions. The coastal regions of Mersin offer ideal conditions in terms of both solar radiation and wind potential. These regions maximize the potential of the hybrid energy system with high annual sunshine duration and suitable wind speeds. In the building design, the panels were positioned to receive solar radiation at the most optimal angle for efficient operation of the solar panels. The panel angles were optimized according to Mersin's latitude and seasonal solar movements. Both fixed-position and solar-tracking systems were evaluated, and the fixed-position system was preferred due to its cost-effectiveness and ease of maintenance. The wind turbine was integrated into the building's roof. This design approach not only saved space but also allowed the turbine to be elevated above the ground, providing access to more stable and stronger wind currents. Integrating the turbine with the building's architecture provided advantages in terms of both visual coherence and aerodynamic performance. This integrated approach combines energy generation and building aesthetics, resulting in an innovative and sustainable design.

The case study building examined in this work is a two-story residential structure located in a rural area of Mersin, designed with a unique architectural approach. The concept designed in the study stands out with its harmony with the environmental context, functional interior arrangements, and energy efficiency-focused details. Modeled using SketchUp software, the structure has a rectangular footprint of 12.07 meters in length and 9.75 meters in width. These dimensions constitute a total base area of 117.68 m². The total height of the structure is set at 2.7 meters, a measure chosen considering human scale and visual balance. The interior layout of the two-story building is designed to support family life. The ground floor is dedicated to common living areas (living room, kitchen, dining area, etc.), while the upper floor contains more private spaces such as bedrooms, bathrooms, and a study area. This floor plan aims to balance privacy and social interaction. Factors affecting the building's energy performance, such as insulation properties, material selection, and window sizes, will be discussed in detail in subsequent sections in the context of simulation results.

Determining the building's energy needs is crucial for sizing the hybrid system and evaluating its performance. In this study, the building's energy demand was approximately calculated considering the widely used TS 825 standard (Thermal Insulation Requirements for Buildings) for residential buildings and empirical data from relevant literature (e.g., Perez-Lombard et al., 2008). The calculations took into account factors such as the building's geographical location (Mersin), climate data (temperature, humidity, solar radiation), building materials, insulation properties (e.g., insulation material and thickness in walls, roof, and floor), window areas (window type and U-value), and lighting and appliance usage (average electricity consumption). The panels, with a slope of 34.75°, were subsequently placed on the model building designed by SketchUp. The spacing of the panels for Mersin province was determined based on calculations. In the study, the building geometry was generated in the SketchUp modeling program. For energy simulation calculations, EnergyPlus was chosen due to its widespread availability, easy access to educational content, calculation capabilities, and interoperability with SketchUp. During the evaluation of the modeled building's energy efficiency,

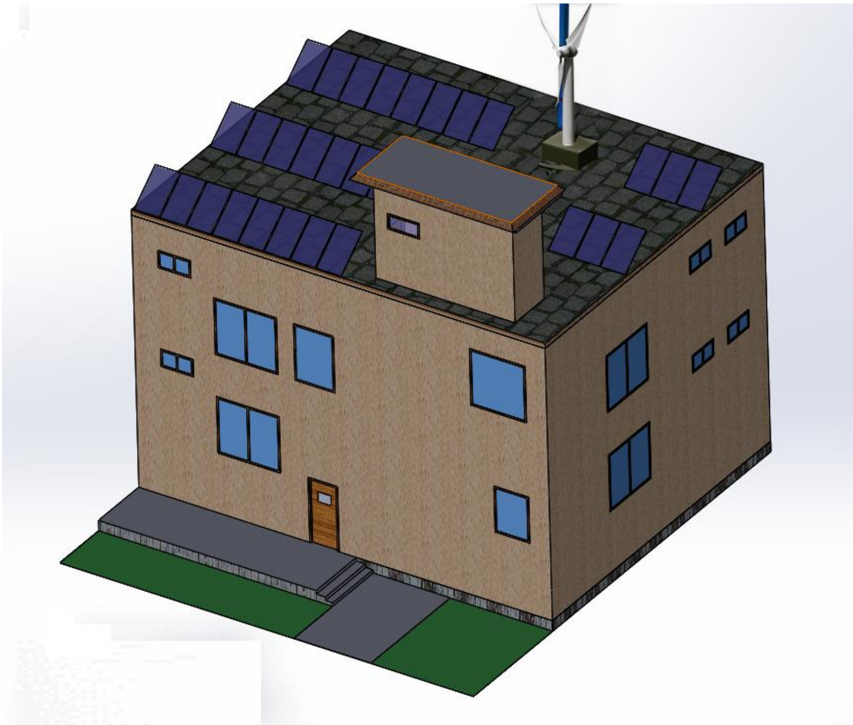

Figure 1: Isometric View of the Case Study Building

Figure 1 represents a modern residential building integrated with renewable energy systems. The design utilizes solar and wind energy (hybrid energy). In the design, a significant portion of the roof is covered with photovoltaic (PV) panels. These panels convert solar energy into electrical energy, meeting a portion of the building's energy needs. The number and arrangement of panels were determined based on the building's energy demand and the region's solar potential. The design includes a vertical-axis wind turbine on the roof. This turbine contributes to the hybrid system by converting wind energy into electrical energy. Vertical axis turbines are preferable in residential applications as they are less sensitive to changes in wind direction.

Building Energy Performance Assessment and Insulation Optimization

In the evaluation of building energy performance, software developed by İzoder (Heat Insulation Association) following solar modeling is frequently preferred today. These types of software, while analyzing the energy efficiency of buildings, allow for the calculation of heat losses through transmission in building elements. These calculations are performed considering the building's insulation properties, the suitability of the materials used, their costs, and environmental impacts. Furthermore, it is also important to ensure compliance with technological advancements in the industry and future energy efficiency targets. Insulation materials used in buildings are evaluated not only for their thermal insulation properties but also according to multifaceted criteria such as fire safety, sustainability (environmental friendliness, recyclability, etc.), and human health.

Insulation in buildings is modeled based on the TS 825 standard (Thermal Insulation Requirements for Buildings) in Turkey. This standard aims to minimize heating and cooling energy consumption by determining the levels of thermal insulation and window properties to be applied in buildings. TS 825, which first came into force in 2000, took a significant step towards increasing energy efficiency in buildings by introducing lower limits for energy demand with the update made in 2008 (Turkish Standards Institution, 2008). TS 825 enables the calculation of annual heating energy demand and the risk of condensation for buildings in four different climate zones of Turkey. These calculations are critically important for evaluating the energy performance of buildings and verifying compliance with legal requirements.

The specific heat loss calculations and condensation data included in the TS 825 standard are used to ensure accuracy and reliability in the evaluation of building energy performance. The building components (walls, roof, floors, windows, etc.) and the materials used are compared with these calculations, and the energy efficiency of the design is reviewed within the framework of national legislation and standards. If the performance criteria determined as a result of the calculations cannot be met, the type of insulation material, thicknesses, layer arrangement, or other design parameters (e.g., window sizes, orientation) are rearranged. According to the calculation method defined in TS 825, the energy performance of the building is evaluated with a holistic approach, taking into account the balance between heat losses and internal heat gains (people, lighting, appliances) and solar energy gain. Among the main factors affecting building energy performance, the physical properties of the structure (dimensions, orientation, surface areas), the efficiency of heating and cooling systems, regional climate conditions (temperature, humidity, solar radiation, wind), and especially the potential of solar energy occupy a large place. Accurate and detailed modeling of these factors is critical for optimizing the annual heating and cooling energy demand of the building and achieving an energy-efficient design.

In this study, EPS (Extruded Polystyrene) was used as the insulation material. Based on the calculations made considering the U-values recommended in the TS 825 standard and relevant literature, optimum insulation thicknesses were determined by taking into account the thermal conductivity coefficients (λ) of the materials used. These calculations aim to optimize the energy efficiency of the building by determining the amount of heat loss from different building elements (walls, roof, floor). Furthermore, insulation materials and thicknesses were re-evaluated by considering environmental factors such as the contact of the building's walls, ceiling, and floor areas with the outside air, open spaces, and soil. This evaluation also includes the condensation control criteria specified in TS 825.

In the thermal performance analysis of the example building, the layered structure of the building elements and the thermal properties of the materials constituting these layers were examined in detail. In this context, thermal resistance (R) values were calculated for each layer of the wall, ceiling, and floor elements, and the total thermal resistance and thermal transmittance (U) coefficients were obtained from these values.

The exterior wall consists of the following layers from inside to outside: internal surface thermal transmittance coefficient, lime mortar, solid or vertically perforated bricks conforming to TS EN 771-1 standard, extruded polystyrene foam (XPS) insulation material, and plaster mortars made of lightweight inorganic aggregates. The thermal resistance of each of these layers was calculated by considering their thicknesses and thermal conductivity values, and the total wall thermal resistance was found to be 2.35 m^2K/W. The corresponding thermal transmittance coefficient was calculated as 0.423 W/m^2K. These values indicate the resistance of the wall to heat transfer and, consequently, its insulation performance.

The ceiling element consists of the internal surface thermal transmittance coefficient, reinforced concrete, and extruded polystyrene foam (XPS) insulation material. The total thermal resistance of the ceiling was calculated as 4.24 m^2K/W, and the corresponding thermal transmittance coefficient is 0.236 W/m^2K. The ceiling, which has a higher thermal resistance compared to the wall, exhibits better thermal insulation performance. This situation is important in terms of reducing heat losses through roofs.

The floor element consists of layers such as the internal surface thermal transmittance coefficient, synthetic material coverings (e.g., PVC), cement mortar screeds, extruded polystyrene foam (XPS) insulation material, another layer of cement mortar screed, and concrete made using non-porous aggregates. The total thermal resistance of the floor was calculated as 2.32 m^2K/W, and the corresponding thermal transmittance coefficient was found to be 0.431 W/m^2K. Due to the more complex heat transfer in soil-contact surfaces and the non-constant soil temperature, a factor of 0.5 is generally used in calculating heat losses through the floor. This factor approximately represents the effect of the soil-contacting surface on heat transfer.

The thermal resistance and thermal transmittance coefficients obtained in this analysis play an important role in evaluating the thermal performance of building elements and calculating building energy performance. Especially the use of insulation materials (such as XPS) significantly increases the thermal resistance of building elements, reducing heat losses.

This situation is of great importance in terms of ensuring energy savings and thermal comfort in buildings.

As a result of the calculations made for the walls of the example building, the total thermal resistance (R) was found to be 2.35 m²K/W. The corresponding thermal transmittance (U) was calculated as 0.423 W/m²K. The total wall area of the building exposed to the outside air was measured as 318 m². According to these data, the total heat loss through the walls was calculated as 134.51 W/K. As a result of the calculations made for the roof of the example building, the total thermal resistance (R) was found to be 4.24 m²K/W. The corresponding thermal transmittance (U) was calculated as 0.236 W/m²K. The total roof area of the building exposed to the outside air was measured as 117 m². According to these data, the total heat loss through the roof was calculated as 27.61 W/K. As a result of the calculations made for the floor of the example building, the total thermal resistance (R) was found to be 2.32 m²K/W. The corresponding thermal transmittance (U) was calculated as 0.431 W/m²K. The floor area of the building in contact with the soil was measured as 117 m². Heat loss calculations for soil-contact surfaces are usually multiplied by a factor of 0.5. Therefore, the total heat loss through the floor was calculated as 25.21 W/K. The total heat loss through transmission from the different building elements (walls, roof, and floor) of the building was calculated as 303.28 W/K, including the heat losses from the exterior windows and doors, using the Izoder program and the calculations mentioned above. This value is an important parameter in evaluating the energy performance of the building. The heat loss from the exterior windows was calculated as 104.9 W/K, and from doors it was calculated as 11 W/K using the Izoder program.

The monthly calculation of the annual heating energy demand of the examined example building provides important information about the thermal performance and energy consumption of the building. In these calculations, the balance between the thermal losses and thermal gains of the building was examined in detail.

The basis of the calculations is the specific heat loss of the building and the difference between the outdoor and indoor temperatures. Specific heat loss refers to the heat loss due to the structural characteristics of the building and the temperature difference between the outdoor and indoor environments. In this study, the specific heat loss was determined as 532.44 W/K. When calculating monthly heat losses, average temperature differences for each month were taken into account. Due to lower outdoor temperatures in the winter months (January, February, November, and December), the temperature differences and consequently the heat losses were found to be higher. For example, the temperature difference determined as 10.6°C in January corresponds to a heat loss of 5,444 W.

The thermal gains of the building were evaluated in two main categories: internal and external sources. Internal heat gains include the heat emitted from the metabolic activities of the occupants, lighting, electrical appliances, and other internal sources. In this study, the average monthly internal heat gain was assumed to be 1,569 W. The most important component of external heat gains is solar energy. Solar energy gain varies depending on factors such as the building's location, orientation, facade characteristics, and monthly sunshine durations. While solar energy gain increases in the summer months, it decreases in the winter months. The sum of these two types of gains constitutes the total thermal gain of the building.

To more accurately reflect the balance between heat losses and gains, correction factors such as the gain utilization factor and the gain coefficient were also included in the calculations. The gain utilization factor indicates how much of the total gain obtained can be effectively used, while the gain coefficient determines the efficiency of gain utilization by considering the thermal inertia and heat storage capacity of the building.

Considering these factors and the heat losses and gains mentioned above, the net heating energy demand of the building for each month was calculated. In the winter months, especially in January and February, the heating demand was higher due to high heat losses and low solar energy gain. In contrast, the heating demand decreased in the spring and autumn months, while there was no heating demand in the summer months (May-September). The heating energy demand for January was calculated as 9,238,572 kJ, 8,168,688 kJ for February, 4,904,728 kJ for March, and 1,109,397 kJ for April. For November, it was found to be 3,884,734 kJ, and for December, it was 8,262,695 kJ. The annual total heating energy demand of the building can be determined by summing these monthly values.

These calculations provide an important basis for determining the measures to be taken to improve the energy performance of the building. Strategies such as improving insulation, making greater use of solar energy, and increasing the efficiency of heating systems can be developed, especially to reduce the high heating demand in the winter months.

RESULTS and CONCLUSIONS

The monthly energy performance of the building examined within the scope of this study provides significant insights into energy efficiency and the utilization of renewable energy sources. The monthly energy performance of the example building was analyzed in detail, considering heating, cooling, photovoltaic (PV) system generation, wind turbine generation, and the amount of electricity drawn from/sold to the grid. The data presented in Table 1 illustrates the building's energy consumption profile, renewable energy generation, and grid interaction in detail.

Table 1: Aylık Enerji Dengesi Tablosu

Month	Heating: EnergyTransfer [kWh](Monthly)	Cooling: EnergyTransfer [kWh](Monthly)	Photovoltaic: ElectricityProduced [kWh](Monthly)	Electricity: Facility [kWh](Monthly)	Electricity Net: Facility [kWh](Monthly)
January	2237.61	0.00	90.45	1889.25	1773.58
February	1550.90	0.00	112.43	1685.78	1556.70
March	412.01	601.00	144.34	1861.94	1701.94
April	0.00	1397.69	163.38	1793.56	1618.33
May	0.00	3410.00	168.07	1889.13	1711.57
June	0.00	5528.67	168.74	1794.96	1615.94
July	0.00	7471.71	153.69	1863.18	1698.94
August	0.00	7506.36	157.82	1889.99	1722.63
September	0.00	5205.07	183.14	1767.92	1574.81
October	0.00	3220.02	124.05	1888.37	1750.76
November	138.97	796.78	129.30	1820.15	1678.93
December	1694.07	0.00	116.32	1835.48	1701.86
Month	WindTurbine: ElectricityProduced [kWh](Monthly)	Electricity: Building [kWh](Monthly)	ElectricitySurplusSold: Facility [kWh](Monthly)	ElectricityProduced: Facility [kWh](Monthly)	ElectricityPurchased: Facility [kWh](Monthly)
January	13.28	1863.70	10.20	115.67	1783.78
February	11.29	1662.58	13.17	129.08	1569.87
March	8.50	1836.89	11.90	160.00	1713.84
April	5.68	1769.85	10.84	175.22	1629.18
May	3.65	1863.70	9.84	177.57	1721.41
June	4.52	1769.85	9.10	179.01	1625.04
July	4.53	1836.89	10.58	164.24	1709.52
August	3.74	1863.70	10.28	167.36	1732.90
September	4.55	1743.03	8.79	193.10	1583.60
October	7.40	1863.70	13.30	137.61	1764.07
November	7.13	1796.66	9.37	141.22	1688.30
December	12.67	1810.07	11.19	133.62	1713.05

When Table 1 is evaluated, it shows the building's energy consumption and production in detail throughout the year. The high heating demand, which becomes evident in the winter months (January, February, November, December), indicates that the building's energy consumption increases during these periods, while the cooling demand, which peaks in the summer months (July, August), points to the intensive use of cooling systems during these months. Renewable energy sources, namely the photovoltaic system and the wind turbine, make significant contributions, especially in the spring and summer months, reducing the amount of electricity the building draws from the grid and even allowing electricity sales to the grid in some months. The "Electricity Net" data in the table clearly show the building's net energy consumption and the impact of renewable energy sources on the energy balance. These data provide an important basis for determining the measures to be taken to increase the building's energy efficiency and optimize the use of renewable energy. The analyses performed comprehensively reveal the contribution of the hybrid energy system under current conditions and the steps that should be taken to increase its efficiency. Figure 2 presents the results obtained regarding the heating and cooling loads of the examined hybrid energy building.

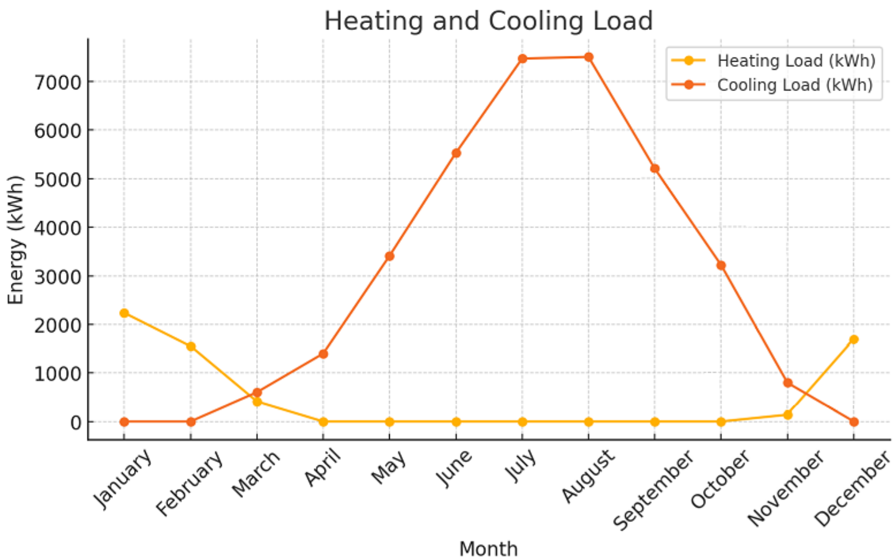

Figure 2: Heating and Cooling Loads

When the heating and cooling loads of the building are examined, the high heating demand in January and February is noteworthy. This situation indicates that the building's energy needs during the winter months are largely due to heating systems. On the other hand, starting from March, the heating load begins to decrease and drops to zero in April. This process reveals that the need for heating disappears in the spring and summer months due to the influence of the Mediterranean climate. Starting from May, cooling loads increase rapidly and peak in July and August (at levels of 7500 kWh). This indicates that a large amount of energy is consumed to maintain comfort inside the building during the summer months due to hot weather conditions. From September onwards, cooling loads begin to decline, and a balance is achieved towards the end of the year as the energy demand decreases again. Figure 3 presents the results obtained regarding renewable energy generation for the examined hybrid energy building.

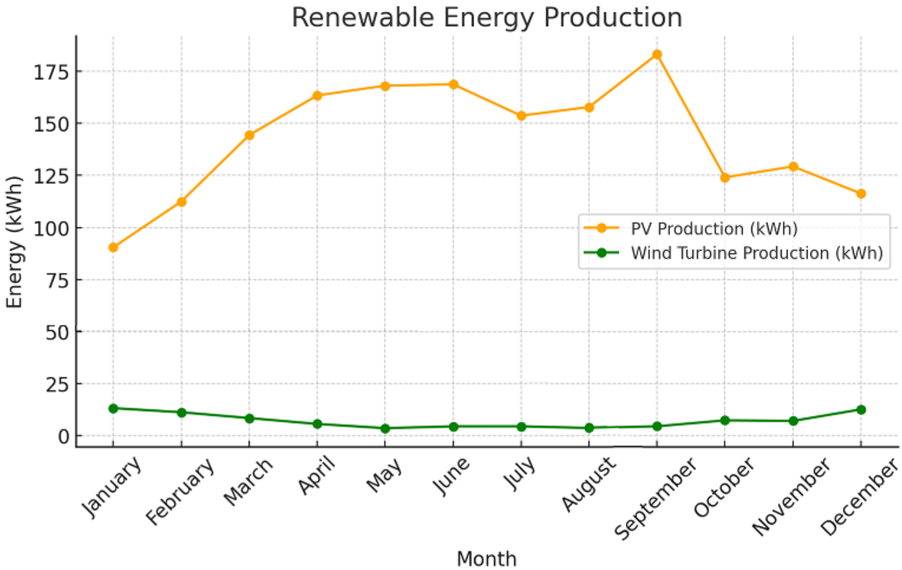

Figure 3: Renewable Energy Generation

Figure 3 illustrates the generation performance of the renewable energy sources used in the system. The solar panels (PV) generate significantly more energy throughout the year compared to the wind turbine. This is due to Mersin being a region with high solar radiation potential. During the summer months, solar panels reach their maximum generation levels, peaking at 183 kWh in September. This indicates that PV panels are more effective in energy generation during the warmer months. The wind turbine, on the other hand, has a lower generation capacity throughout the year. The average monthly energy generation varies between 3-12 kWh, a contribution that is quite limited compared to solar panels. This situation highlights the importance of using the wind turbine as a supplementary energy source. Figure 4 presents the results obtained regarding the facility's consumption and the electricity drawn from the grid for the examined hybrid energy building.

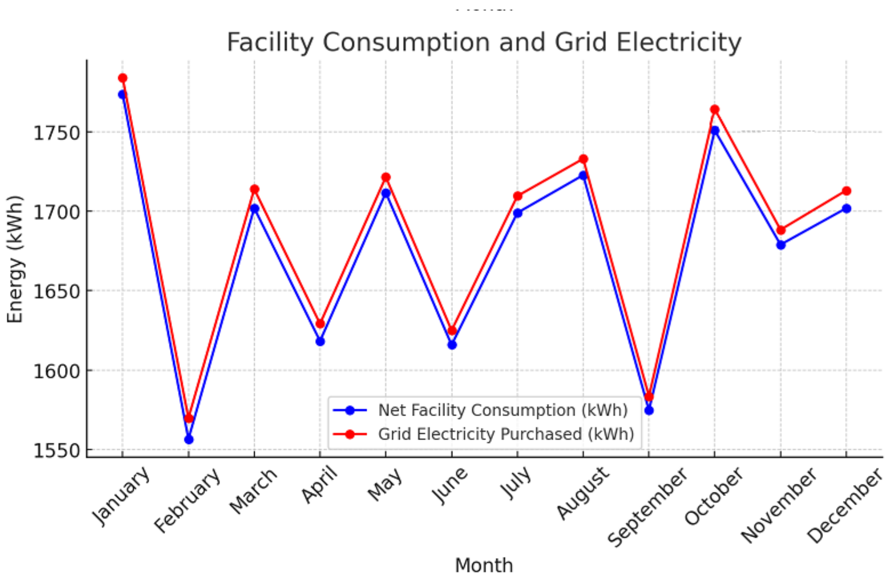

Figure 4: Facility Consumption and Electricity Drawn from the Grid

When Figure 4 is examined, it compares the facility's net energy consumption and the amount of electricity drawn from the grid, revealing that energy generation is insufficient to meet consumption. Particularly during the summer months, due to the increased cooling demand, a significant increase in the amount of electricity drawn from the grid is observed. This situation demonstrates that the renewable energy system alone cannot meet the entire energy demand and that grid support is still a significant necessity. Throughout the year, the amount of electricity drawn from the grid follows a parallel trend with the facility's energy consumption. This indicates an existing imbalance between energy generation and consumption and suggests that the hybrid system needs to be made more efficient. Figure 5 presents the results obtained regarding the comparison of renewable generation and consumption for the examined hybrid energy building.

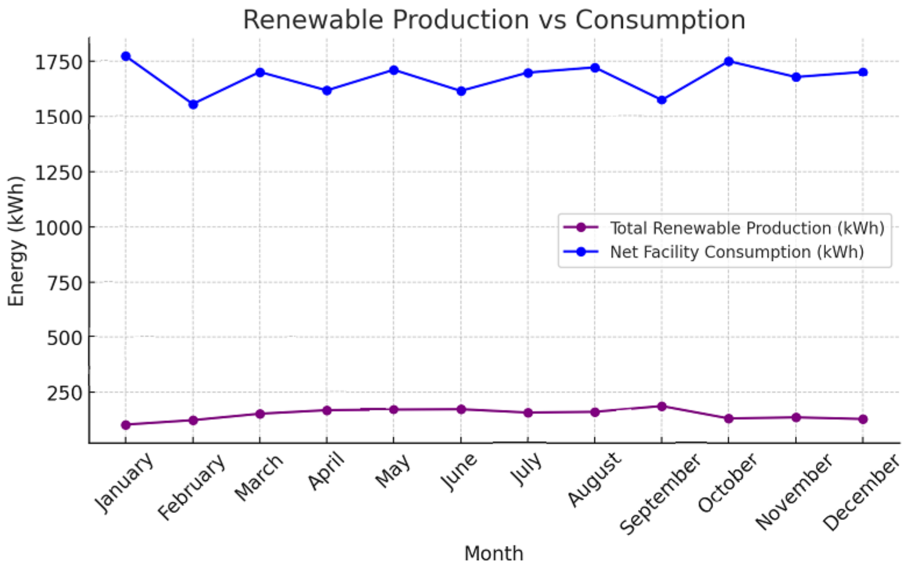

Figure 5: Comparison of Renewable Generation and Consumption

Figure 5, which compares renewable energy generation with the facility's total energy consumption, reveals that the system's current generation capacity is far from meeting the consumption. The combined generation of PV panels and the wind turbine falls significantly short of meeting the increased cooling load, especially during the summer months. This situation highlights the necessity of incorporating additional energy generation sources into the system. To enhance the performance of the hybrid system, particularly during periods of peak energy demand in the summer months, increasing the number of PV panels and integrating a more efficient wind turbine can be considered. Additionally, increasing the capacity of energy storage systems is important for utilizing the generated energy more efficiently.

These results indicate that the energy generation capacity of the hybrid system should be increased and that the balance between consumption and generation should be optimized. The following suggestions stand out:

Solar energy generation can be increased by using more PV panels.

The use of more efficient or a greater number of wind turbines can increase energy generation.

Increasing battery capacity will help balance fluctuations between energy generation and consumption.

Smart energy management systems and energy-saving measures can contribute to optimizing energy demand.

These analyses demonstrate that hybrid energy systems offer a significant solution for energy efficiency and sustainability in regions with high renewable energy potential, such as Mersin.

REFERENCE

Al-Ghussain, L., Samu, R., Taylan, O., & Fahrioglu, M. (2020). Sizing renewable energy systems with energy storage systems in microgrids for maximum cost-efficient utilization of renewable energy resources. Sustainable Cities and Society, 55, 102059.

Assaf, J. (2018). Integrated solar-hydrogen combined heat and power/solar-thermal systems for power and hot water supply in standalone applications (Doctoral dissertation, RMIT University).

Bakić, V., Pezo, M. L., Jovanović, M. P., Turanjanin, V., Vučićević, B. S., & Mirkov, N. S. (2012). Technical analysis of photovoltaic/wind systems with hydrogen storage. Thermal science, 16(3), 865-875.

Bakić, V., Pezo, M. L., Jovanović, M. P., Turanjanin, V., Vučićević, B. S., & Mirkov, N. S. (2012). Technical analysis of photovoltaic/wind systems with hydrogen storage. Thermal science, 16(3), 865-875.

Bhatti, S., Manzoor, H. U., Michel, B., Bonilla, R. S., Abrams, R., Zoha, A., ... & Ghannam, R. (2022). Machine learning for accelerating the discovery of high performance low-cost solar cells: a systematic review. arXiv preprint arXiv:2212.13893.

de Campos Souza, P. V. (2020). Fuzzy neural networks and neuro-fuzzy networks: A review the main techniques and applications used in the literature. Applied soft computing, 92, 106275.

Esmaeilishayan, M., Najafi, G., Ghobadian, B., Gorjian, S., & Mazlan, M. (2022). Sustainable design of a near-zero-emissions building assisted by a smart hybrid renewable microgrid. International Journal of Renewable Energy Development, 11(2), 471-480.

Gadkari, S. A. (2008). A Hybrid Reconfigurable Solar And Wind Energy System (Doctoral dissertation, Cleveland State University).

Güven, A. F., & Mete, M. K. (2021). Balıkesir'in Erdek İlçesi için Şebeke Bağlantılı Hibrit Enerji Sistemi Fizibilite Çalışması ve Ekonomik Analizi. Mühendis ve Makina, 63(706), 138-158.

Hassan, Q., Algburi, S., Sameen, A. Z., Salman, H. M., & Jaszczur, M. (2023). A review of hybrid renewable energy systems: Solar and wind-powered solutions: Challenges, opportunities, and policy implications. Results in Engineering, 101621.

Hosseini, E. (2023). Tri-Level Model for Hybrid Renewable Energy Systems. arXiv preprint arXiv:2312.03776.

Isabel Abreu, M., Corvacho, H., & P. Dias, R. (2011). Passive systems for buildings using buoyancy-driven airflows. Recent patents on engineering, 5(1), 23-31.

Işık, E., Ün, B., Mıstıkoğlu, G., & Erdiş, E. (2023). Yapı Sektöründe Yenilenebilir Enerji Kaynaklarının Kullanımı. Conference Paper in International Conference on Applied Engineering and Natural Sciences · July 2023 DOI: 10.59287/icaens.1089

Kara, M., Ercan, Y., Yumuşak, R., Cürebal, A., & Eren, T. (2022). Yenilenebilir Hibrit Enerji Santrali Uygulamasında Tesis Yer Seçimi. International Journal of Engineering Research and Development, 14(1), 208-227.

Mokhtara, C., Negrou, B., Bouferrouk, A., Yao, Y., Settou, N., & Ramadan, M. (2020). Integrated supply–demand energy management for optimal design of off-grid hybrid renewable energy systems for residential electrification in arid climates. Energy Conversion and Management, 221, 113192.

Mokhtara, C., Negrou, B., Settou, N., Settou, B., & Samy, M. M. (2021). Design optimization of off-grid Hybrid Renewable Energy Systems considering the effects of building energy performance and climate change: Case study of Algeria. Energy, 219, 119605.

Nnadi, D. B., Odeh, C. I., & Omeje, C. (2014). Use of hybrid solar-wind energy generation for remote area electrification in South-Eastern Nigeria. Journal of Energy in Southern Africa, 25(2), 61-69.

Nyemba, W. R., Chinguwa, S., Mushanguri, I., & Mbohwa, C. (2019). Optimization of the design and manufacture of a solar-wind hybrid street light. Procedia Manufacturing, 35, 285-290.

Ridha, H. M., Gomes, C., Hizam, H., Ahmadipour, M., Heidari, A. A., & Chen, H. (2021). Multi-objective optimization and multi-criteria decision-making methods for optimal design of standalone photovoltaic system: A comprehensive review. Renewable and Sustainable Energy Reviews, 135, 110202.

Roy, P., He, J., Zhao, T., & Singh, Y. V. (2022). Recent advances of wind-solar hybrid renewable energy systems for power generation: A review. IEEE Open Journal of the Industrial Electronics Society, 3, 81-104.

Samek, W., Montavon, G., Lapuschkin, S., Anders, C. J., & Müller, K. R. (2021). Explaining deep neural networks and beyond: A review of methods and applications. Proceedings of the IEEE, 109(3), 247-278.

Savaş, S., Duraklar, K., Çınar, O. A., Koç, M., Turan, A., Uslu, U., ... & Duşbudak, H. (2022). Güneş enerjisi sistemlerinde yenilikçi ve akıllı bakım onarım. Journal of Information Systems and Management Research, 4(2), 35-49.

Trimble. (2021). SketchUp Pro Retrieved from https://www.trimble.com.

Türk Standartları Enstitüsü. (2008). TS 825: Binalarda Isı Yalıtım Kuralları ve Hesaplamalar. Ankara: Türk Standartları Enstitüsü.

U.S. Department of Energy. (2021). OpenStudio. Retrieved from https://www.openstudio.net

U.S. Department of Energy. (2024). EnergyPlus Engineering Reference. Available at https://energyplus.net

Vadakkepurakkel, A. K. (2019). Design of a hybrid power generation system using solar-wind energy (Doctoral dissertation, Deakin University).

van Schijndel, A. W. M. (2016). BES with FEM: Building Energy Simulation using Finite Element Methods. arXiv preprint arXiv:1606.01243.

Yildiz, C. (2024). Binalarda Enerji Verimliliğinde Son Gelişmeler: Türkiye Örneği. Gazi University Journal of Science Part C: Design and Technology, 1-1.

The Cost Analysis of Conversion from Fossil Fuel Vehicles to Electric Vehicles

İrfan MACİT[1]

1- Öğr. Gör. Dr.; Çukurova Üniversitesi Mühendislik Fakültesi Endüstri Mühendisliği Bölümü. irfanmacit@gmail.com ORCID No: 0000-0001-5966-5726

ABSTRACT

Internal combustion fossil fuel passenger vehicles are scrapped after their engine failures cannot be fixed or after their economic life. If some of these vehicles only have engine hardware failures and their running hardware is functional, there is an economic loss. It is possible to convert such vehicles into electric vehicles by installing appropriate electrical equipment. Thus, vehicles with such problems can be brought back to the economy by converting only the internal combustion engine to an electric motor (ICE) under suitable conditions. In this study, it was investigated whether it is economical to convert internal combustion fossil fuel vehicles (ICE) to electric vehicles (EV) and how long it will take to cover the investment cost if the conversion is made. The scope of the study was narrowed down by considering passenger type internal combustion mid-range vehicles. The proposed calculation method is aimed to help in the conversion of internal combustion engines to electric vehicles. It is expected that the data obtained as a result of the study will be used in conversion calculations and will open wide research area for new studies.

Keywords – Internal Combustion Engine, Electric Vehicle Conversion, Cost Analysis, Berak-point Analysis, Breakeven Analysis.

INTRODUCTION

In recent years, the automotive industry's focus has significantly shifted towards the rapid increase in the production of electric vehicle (EV) models. Historical records suggest that the invention of electric vehicles dates back to nearly two centuries ago, initiated by Faraday's theory of electromagnetism. While it is believed that the first electric vehicles were invented in the early 1830s, there is no definitive consensus on the inventor, and some sources present conflicting information.

The negative impact of internal combustion engines (ICEs) on the environment and human health due to particle and gas emissions is well-documented (Zainuri et al., 2024). Converting conventional vehicles to electric ones involves replacing the internal combustion engine with an electric motor and components powered by electrical energy.

Today, electric vehicle conversions are predominantly observed in passenger cars, light commercial vehicles, and heavy-duty vehicles. As of 2023, the estimated number of road vehicles globally is approximately 2.24 billion, in addition to marine and air vehicles used for various purposes. In Turkey, according to the Turkish Statistical Institute (TÜİK), the number of registered vehicles reached an all-time high of 28,740,492 in 2023, with a distribution as detailed in Table 1.

Table 1. Proportional Distribution of Land Vehicles in Turkey in 2023

Vehicle Type	**Proportion (%)**
Passenger Car	53.0
Motorcycle	17.7
Light Commercial	15.6
Tractor	7.6
Truck	3.3
Minibus	1.8
Bus	0.7

As shown in Table 1, passenger cars make up the majority of these vehicles. With the increase in the number of vehicles, the demand for fuels used in their systems also rises. Fossil fuels such as gasoline, diesel, liquefied natural gas (LNG), and compressed natural gas (CNG) are commonly used in ICE-powered vehicles, while experimental hydrogen fuel cell ICEs are excluded from this study.

Numerous studies in the literature highlight the environmental consequences of greenhouse gases emitted by fossil fuels, which contribute to climate change. With countries promoting cleaner energy sources, electricity, which is less polluting than fossil fuels, has started to be used in vehicles. Over the past two decades, the use of electricity in land, air, and marine transportation has gained significant traction. For road vehicles, in particular, electric energy usage aligns better with market expectations in terms of efficiency.

The propulsion system in electric vehicles relies on an electric motor powered by a battery installed in the vehicle. However, battery capacity remains a constraint for EVs. As advancements in battery technology continue, this limitation is expected to diminish.

Converting ICE-powered vehicles to electric involves complying with technical requirements and legal regulations, such as obtaining type approval documents for vehicle registration. When performed in adherence to these rules, the conversion process can significantly benefit the economy. Moreover, as fossil fuel resources dwindle, vehicles that rely on these fuels may lose value and become obsolete. By replacing the propulsion mechanisms of fossil-fuel vehicles with electric motors, their economic life can be extended. In the future, new regulations might even make such conversions mandatory.

This study examines the economic analysis of converting fossil fuel-powered vehicles to electric by replacing ICE mechanisms with electric motors to extend their economic life. The analysis is conducted using engineering economics techniques.

Electric Vehicle in Literature Short Review

The invention of the first electric vehicles involved battery replacement when the energy was depleted, as there was no charging system to recharge the batteries while in use. This limitation persisted until 1859, when physicist Gaston Plante invented rechargeable batteries. Later, in 1881, French chemical engineer Camille Alphonse Faure developed a method for mass-producing lead-acid batteries, giving electric vehicles a new dimension. However, battery capacity has continued to limit the performance of electric propulsion systems to this day. Hybrid propulsion systems that partially utilize both fossil fuels and electricity were developed to address these constraints.

Hybrid Electric Vehicles

Hybrid vehicles are equipped with both electric motors and internal combustion engines as propulsion systems. At lower speeds and torque demands, the vehicle uses electric energy, while higher speeds and loads activate the ICE. The battery system in hybrid vehicles is charged either through the ICE's motion or internal mechanisms.

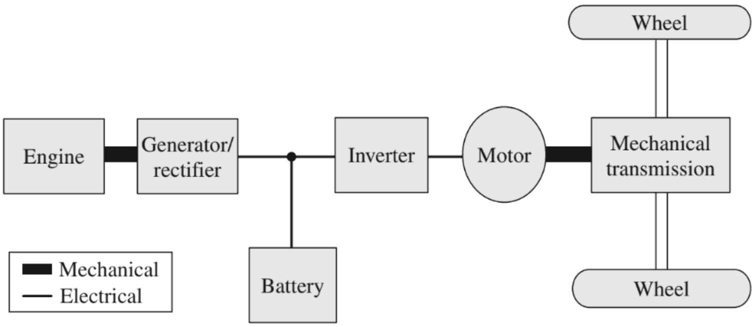

Figure 1: Hybrid Electric Vehicle, (Mi & Masrur, 2017)

Fully Electric Vehicles

Fully electric vehicles (EVs) are land vehicles in which the propulsion energy is entirely provided by an onboard battery. The required energy is supplied by an electrical battery cell and a power management unit. Battery charging is generally performed using devices connected to the electrical grid, though solar-powered charging stations are also available in some cases.

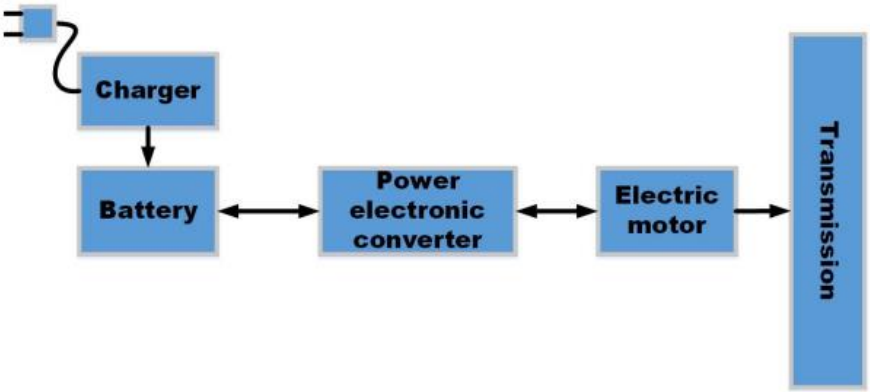

Figure 2: Fully Electric Vehicle Architecture, (Ehsani et al., 2021)

Electric Vehicle Conversions

Countries are introducing environmentally conscious legal frameworks to make land vehicles more eco-friendly in the future. Reducing carbon emissions in transportation aligns with these sustainability goals. Additionally, the depletion of fossil fuel resources is gradually necessitating a reduction in ICE usage. Abruptly decommissioning a large number of ICE vehicles would negatively impact national economies and consumer budgets. Vehicles rendered obsolete might lead to economic losses and social challenges. To address these issues, converting ICE vehicles to electric ones ensures their continued economic value.

Electric vehicle conversions are conducted using standardized conversion kits developed by various manufacturers. These kits are tailored to vehicle weight, range, comfort, technology, and technical constraints. Conversion designs must also consider battery charging methods and types, as some batteries require alternating current (AC) while others use direct current (DC). Home-based charging typically takes 8–12 hours for a full charge, while high-capacity fast chargers at stations can charge up to 80% in 20–45 minutes, depending on the system.

Every conversion project requires a detailed calculation of investment and maintenance costs. For example, replacing an ICE with an electric motor varies in cost depending on whether the motor is connected to the existing transmission or directly to the wheel axles. Additional considerations include chassis design, front/rear-wheel drive configuration, and required customization.

METHODOLOGY

Electric vehicle (EV) conversions are conducted using standardized units known as electric vehicle conversion kits. Manufacturers prepare these kits based on the specific weight, range, comfort, technological, and technical constraints of the vehicle. Additionally, manufacturers can offer customized kits tailored to consumer preferences. The design of vehicle battery systems is also a crucial aspect of the conversion process, as some battery systems are compatible with alternating current (AC) charging, while others require direct current (DC).

The time required for a complete conversion depends on the vehicle's specifications. Each component being replaced or removed, such as the internal combustion engine (ICE), gearbox, axles, braking systems, and fuel systems, demands specific labour hours, as shown in Table 2.

Table 2. Labor Time for Removing Vehicle Components During EV Conversion

Internal Combustion Engine	**120**
Transmission	40
Front Axles	30
Rear Axles	40
Brake System	80
Air Conditioning System	30
Fuel Tank and System	60
Low-Voltage Wiring	100
Internal Combustion Engine	120

Since the processes involved in the removal of internal combustion engines are generally similar, the unit costs tend to be close to each other. These processes only involve disassembly, and no modifications are made to the components of the internal combustion engine that will be reinstalled. The disassembly of internal combustion engines relies more on experience than on advanced technical knowledge and skills. Moreover, even though the dismantled internal combustion engines may be scrapped, they still hold economic value, which falls outside the scope of this study. To ensure the continued economic lifespan of the internal combustion engines being removed, the disassembly must be performed by a specialist.

Table 3. Labor Time for Installing Components in EV Conversions

Component	Time Required (Person-Minutes)
Electric Motor	120
Electric Inverter	60
Motor and High-Voltage Wiring	120
Battery System	120
Battery Modules	200
New Brake System	180
Low-Voltage Wiring Revisions	150
Air Conditioning and Climate Control	120
Vehicle Control Unit Modifications	180
Electric Motor	180
Electric Inverter	150
Motor and High-Voltage Wiring	240

The removal of internal combustion engines from vehicles and the installation of electric motors for electric vehicle conversions may not be completed solely through assembly. Some electric motors require modifications to fit the vehicle's axles. In these cases, electric vehicle motor manufacturers typically provide standard revision parts and conversion kits along with the electric motors. However, these parts often do not fully match the vehicles, requiring additional revisions.

Each revision results in extra labour and manufacturing costs, in addition to the standard unit times listed in Table 3.

Vehicle engine replacement labour costs can be divided into fixed and variable costs. Fixed part replacement costs refer to the preparation costs for adapting the vehicle, which remain constant for every vehicle. Examples of these include preparing the vehicle for conversion, such as removing the engine hood, seats, and doors. These labour costs are considered fixed for all parts replaced and are added as part of the vehicle's fixed costs.

Table 4. Labour Time for Installing Components in EV Conversions

	Unit Conversion Probality	
Components	Worst Case	Best Case
Electric Motor	0.65	0.10
Electric Inverter	0.65	0.05
Electric Motor Revise Labour	0.70	0.05
Electric Motor High Power Cable Setup	0.70	0.05
Battery Setup	0.80	0.10
Battery Unit / Modul	0.70	0.10
Brake System (**New Setup**)	0.80	0.05
Brake System Revise (old System)	0.70	0.05
Air Condition System Setup	0.70	0.05
Car Control System Unit (ECU) Setup & Revise	0.40	0.01
Steering Revise	0.50	0.05
Low Power System Setup & Revise	0.80	0.10

Table 5 presents the annual failure rates of components for an electric vehicle. These rates provide an approximate indication of how likely various components are to fail during the vehicle's lifespan. However, these rates can vary based on factors such as the vehicle's usage patterns, duration of use, personal preferences, operating climate, and intended purpose.

Table 5. Probability of Electric Vehicle Component Failure

Components	Expected Prob. Of Faulty (Years)	Exlanation of Faulty
Battery	%1-3	Electric vehicle batteries usually lose capacity rather than fail. Passenger cars have longer warranty periods.
Elektric Motor	%0.5-2	The engines of electric vehicles are more durable than other electric motors and generally have a low failure rate.
Charge System	%2-5	The possibility of an electric vehicle home charger malfunctioning is common due to the frequency change in the mains voltage. Since general charging units are more tightly controlled, these types of chargers and their ports are less likely to malfunction. However, it may also vary depending on the charging habits of the user.
Power Elecreonics	%1-4	Electric vehicle DC/DC converters and inverters may also experience failures caused by grid voltage frequency fluctuations and sudden and high voltage instability.
Heat pump	%2-6	Control system, circuit failure, and sensor error encountered in the thermal management system of the battery of electric vehicles may cause problems in battery usage.
Sensors & Suspension	%3-7	Geographical and harsh road conditions and climate-related environmental effects may affect the proper use of the vehicle's sensor and suspension systems.
Break System	%1-3	By using the electro-mechanical and regenerative braking system found in electric vehicles, brake pad and disc wear is relatively less than in the conventional braking system.
Software and Eelctronics	%5-10	The most common problems encountered in electric vehicles are software and update errors, software hardware incompatibilities, and battery management system software being incompatible with usage. These faults are seen in almost all electric vehicles.

The change possibilities of faults that may occur in an electric vehicle, as well as their frequency, can be explained as seen in Table 6 below. According to this table, in addition to the occurrence of a fault during the operation of an electric vehicle component, another issue that should be considered is how frequently these faults will occur. Accordingly, the frequency of faults generally varies depending on the use, as seen in the description of the component.

Table 6. Frequency of Failures in Electric Vehicles

Components	Freq. of Faulty	Cause of Failures	Explanation
Battery	Low-Mid	Cell failure, cooling related problems, thermal runaway and leakage	The battery warranty period is generally 8-10 years. In most cases, capacity loss is more common than failure.
Elektri**c** Motor	Very Low	Motor bearing wear, insulation leakage and deterioration	DC/AC Electric motors are much less complex and durable than internal combustion engines.
Charge System	Mid	Charging port deformation issues, updated software required	Malfunctions in home or fast chargers may depend on usage habits.
Power Electronics	Low-Mid	Unbalanced voltage stress due to frequency change, heat pump and cooling problems	Although DC Inverters and converters (DC-DC) are generally reliable, overloads can create high risks.
Heat Pump	Mid	Measurement error or fan failure due to pump, signal control system problems	The thermal management hardware and software of the battery on the vehicle is a critical component, any failure may affect the life of the battery operating in the system.
Suspension & Sensors	Mid-High	Deformations, factors related to the environment used, incorrect measurements of sensors	Sensor errors are frequently encountered in autonomous driving or advanced driver assistance systems of vehicles.
Break System	Low-Mid	Problems with regenerative braking systems for electric motors	Compared to conventional brakes, the pads wear less, but electro-mechanical failures may occur in the regenerative system.

Software And Electronics	Mid	Software update errors, version incompatibilities, socket connection problems	As the complexity of vehicle software increases, the number of errors that may occur may increase, and incompatibilities may occur due to changes in communication protocols.

In electric vehicles, the power required for the motors to move is provided by the vehicle's battery. In calculating the battery life, the usage conditions, charging-circulation habits, charge retention rate (SoC), climate conditions and battery chemical properties can be considered as critical factors. Some formulas are used to calculate the useful life of an electric vehicle battery. The most commonly used model is the calculation method where the battery charge cycle is taken as a reference (Yoshio et al., 2009).

$$T_c = \frac{B_{cap}(kWh)}{U_{cap}\left(\frac{kWh}{cycle}\right)} \tag{1}$$

In this total charge cycle T_c calculation method, B_{cap} is the battery capacity in kWh, U_{cap} is the amount of capacity used in each charge cycle in kWh/cycle. In general, when the number of cycles T_c is completed, the battery capacity is expected to drop to 80%. One of the basic methods that calculates the capacity loss in batteries is the Peukert method. According to this method, Equation (2) is the model that explains the capacity loss depending on the discharge rate of the battery (Hausmann & Depcik, 2013).

$$Q = C\left(\frac{I}{I_{nom}}\right)^k \tag{2}$$

According to Equation (2), where Q is the usable capacity of the battery, C is the nominal capacity of the battery, I is the drawn charge current and I_{nom} is the nominal capacity. Another factor affecting the amount of battery loss is high temperature, which causes permanent loss of charge capacity of the batteries. Such battery capacity losses are called thermal losses or thermal degradation. The Arrhenius model is used as the most well-known calculation method in calculating the degradation capacity losses of batteries (Liu et al., 2010).

$$k = A.e^{\frac{E_\propto}{RT}} \tag{3}$$

In the battery degradation model, equation (3) is calculated using k as the reaction rate constant, $E_\propto$ as the activation energy constant, R as the gas constant and T as the temperature in kelvin (K). When all these calculation methods are considered, it is seen that the service life of electric vehicle batteries does not depend on a single factor, but their capacities also vary. If we assume that the daily capacity of a Li-ion battery with a nominal capacity of 120 kWh is 100 kWh, the economic service life can be calculated as an average of 3000 cycles as follows.

$$T_c = \frac{B_{cap}(kWh)}{U_{cap}\left(\frac{kWh}{cycle}\right)} = \frac{3000}{\frac{365}{(120/100)}} \cong 9{,}9\ years$$

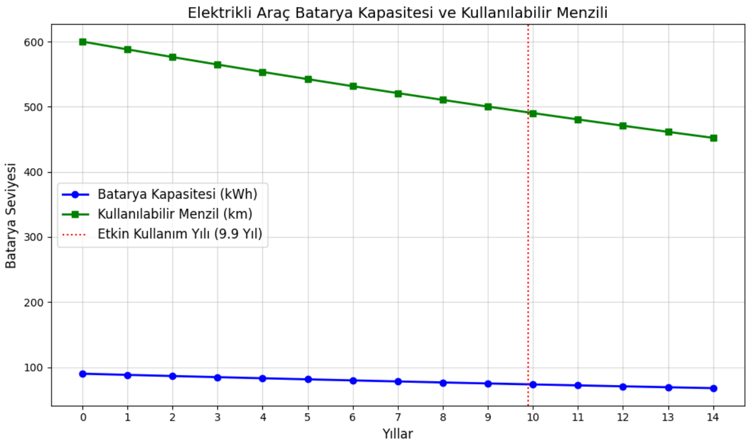

Figure 3. Electric Vehicle Battery Capacity Based Usage Graph

The battery capacity loss in the Peukert calculation of an electric vehicle that operates with a 2% loss each year will be as in Figure 3.

For the economic analysis comparison of the conversion of electric vehicles, the probabilities of failures that may occur in internal combustion engine vehicles and their frequencies should also be taken into account. Internal combustion engine vehicles are more likely to fail than electric vehicles due to their complex engine and drive systems. In general, the annual failure probabilities of a passenger type internal combustion vehicle are at different rates as seen in Table 7.

Table 7. Probality of Failure in Internal Combustion Vehicles

Components	**Probality of Failure (Years)**	**Explanation of Faillures**
Motor (ICE)	%5-10	It varies depending on factors such as lack of engine lubrication, engine block thermal stress, and mechanical wear.
Gearbox/Transmission	%3-5	The probability of failure may be higher in electro-mechanical and automatic transmissions due to oil and sensor-related failures, and lower in manual transmissions.
Fuel System	%5-8	This rate may be caused by the low quality fuel used by the engine, and may increase further if the fuel filter is not replaced and maintained properly.
Exhaust	%3-6	Problems occur more frequently in the catalytic converter system, which filters bad gases while the exhaust gases of the vehicle engine are being thrown out, and in the oxygen sensors connected to it, and in leaks due to rust and corrosion in the exhaust system.
Motor Fluid System	%8-12	Lack of liquid coolant, radiator deformation, coolant pump failures are generally common. Coolant should be changed regularly.
Electric System	%10-15	Frequent battery use due to systems such as start-stop in passenger vehicles, selection of an inappropriate battery capacity, and the service life of the alternator and starter motor components depend on it.
Suspension & Sensors	%5-10	Sensors are affected by environmental factors such as climate and geographical conditions, and excessive loads and improper use of the vehicle reduce the life of the suspension system.
Break System	%5-8	It occurs due to traditional brake disc and pad wear, regular change of brake system fluid and maintenance of brake system channels are required.
TurboCharge	%5-10	It is necessary to regularly maintain the turbocharger lubrication system and clean the dirt in the turbo vane system, otherwise the probability of failure increases.
Clutch (If Manual Systems in)	%10-15	If a vehicle has a manual transmission, the risk of mechanical fasteners malfunctioning increases due to frequent and heavy traffic use.

The engine structure in internal combustion engine vehicles consists of more parts compared to electric vehicles. This complexity increases even more when the different combustion patterns of fuels in their own combustion chambers are taken into account, especially because the engine fuel system is diesel, gasoline or LPG. However, as can be seen from Table 8, the fact that the engine fuel intake systems in internal combustion engine vehicles are atmospheric or turbocharged (high intake air pressure systems such as superchargers etc.) increases this complexity and the probability and frequency of failure.

Table 8. Failure Frequencies of Internal Combustion Engine Vehicles

Components	**Freq. of Faillure**	**Cause of Faillures**	**Explanation**
Motor (ICE)	Mid-High	Overheating, lack of lubrication, piston or cylinder damage	It is generally caused by not changing the engine's regular oil maintenance, filter, or not preventing oil leaks, which is critical for the engine.
Gearbox/Transmission	Mid	Gear wear, lack of oil and hydraulic fluid, electronic control card failures	It is caused by sensor and electronic card failures of automatic and electromechanical transmissions, unsuitable oil and hydraulic fluid damages the cards and sensors, so the failure rates are higher than manual transmissions.
Fuel System	Mid	Fuel pump failure, injector blockage	Inadequate fuel quality or failure to change the fuel filter during maintenance may cause this. Especially low quality fuel damages the injectors.
Exhaust System	Mid	Catalytic converter blockage, sensor failures	In diesel-fueled vehicles, failure to clean the DPF in particular causes frequent failure of the exhaust gas recirculation (EGR) valve and oxygen sensor. At the same time, pollutants released from low-quality fuel also cause additional failures.
Motor Fluid System	High	Radiator leaks, water pump failure	Engine overheating is caused by inadequate coolant, replacing it with mains water, or leaks in the liquid hose. This is the most important issue to be considered during maintenance, especially when climate conditions change.
Electric System	Mid	Battery problems, alternator failure, ignition system problems	Battery life may vary depending on climate conditions. This is due to the lack of necessary tests during maintenance.
Suspension & Sensors	Mid-High	Wear and tear, environmental effects	It is one of the types of failures caused by geographical region and driving habits. It often occurs

			in rough and careless use.
Break System	Mid	Disc and pad wear, hydraulic fluid leaks	Since there is no regenerative braking system in internal combustion engine vehicles, brake discs and pads wear out faster. This is caused by improper and untimely replacement of brake hoses and brake fluid during maintenance.
Turbocharge (in System)	Low-Mid	Overload, lack of lubrication	The turbocharger lubrication system is more common in some engines due to the negativities caused by oil maintenance. It can also be caused by not performing EGR maintenance on time in diesel vehicles.
Clutch (If in Manuel **System)**	Mid-High	Disc wear, hydraulic failures	It is a very common malfunction in vehicles used in heavy traffic conditions.

In general, the complex structure of internal combustion engines is another important factor that increases maintenance costs. The presence of many parts in these types of engines, mechanisms such as different types of fuel systems, also causes maintenance costs to increase rapidly. In order to reduce maintenance costs, it is necessary to keep these systems under constant control. Since mechanical moving engine parts or electro-mechanical parts face high wear and tear as a result of their continuous operation, they also create maintenance cost risks. In addition, malfunctions of electronic systems, control circuit cards and sensors or failure to work as a result of electrical fluctuations increase the risk of malfunctions and damage.

Other economic analysis parameters in the conversion of internal combustion vehicles to electric vehicles are the periodic maintenance costs that occur during the use of the vehicles. These costs occur according to certain probabilities as in Table 6, and in some cases, they can be at a certain time frequency, usually annual. These costs are the maintenance costs encountered during the economic life of the vehicles and are carried out to protect the economic values of the vehicles. Periodic maintenance and operating costs prevent the economic value of vehicles from decreasing, and also ensure that vehicles can be driven safely without losing their economic value. The approximate calculation of maintenance costs consists of the average unit costs shown in Table 9.

Table 9. Vehicle Periodic Maintenance Costs Sample Comparison Table

Service **1400cc ICE**	**Types**	Unit average labour times (km)/year			
		0-10.000 1 year	10.001-100.000 2 years	100.001-200.000 2-5 years	200.001> 5 -10 years
ICE (fuel)		1000 USD	4000USD	3000USD	6000USD
ICE (diesel)		2000USD	8000USD	10000USD	15000USD
EV Hybrid		2000USD	2000USD	6000USD	10000USD
EV		2500USD	3000USD	8000USD	10000USD

There are various methods for calculating power in internal combustion fossil fuel vehicles. These methods are calculated differently depending on the type of vehicle, production purpose and usage purpose. Similarly, there are various methods for calculating power in electric vehicles. Power calculations in internal combustion fossil fuel vehicles and electric vehicles can be made in common units, kW and horsepower. Since these technical calculations are outside the scope of the study, it is necessary to briefly mention that the torque power of the electric motor is multiplied by the speed of the electric motor and the result is divided by 5252 to obtain the horsepower of the engine.

Direct motor driven systems

In direct motor-wheel drive systems, the converted motor of the vehicle is directly connected to the vehicle's axles. The electric motor rotor transmits power directly to the vehicle wheels with the help of two different types of connection elements, with or without a reduction gear. Despite the cost advantage and ease of application, it is not preferred due to the overloading of electric motor control systems.

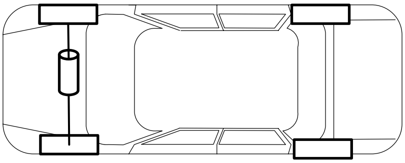

Figure 3. Direct Drive Front Wheel Drive Electric Vehicle Model

In the direct front-wheel drive electric vehicle model, the electric motor is designed as in Figure 3 and the electric motors are connected to the front wheels of the vehicle via axles. This design is the most preferred design model in terms of ease of application and cost.

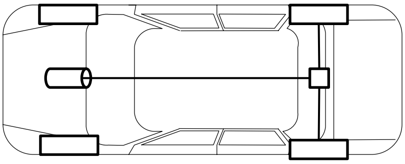

Figure 4. Direct Drive Rear Wheel Drive Electric Vehicle Model

In the direct rear-wheel drive electric vehicle model, the electric motor is designed as in Figure 4 and the electric motors are transferred to the rear wheels of the vehicle via a differential transmission system. Unlike this design, there are shaft and differential drive systems in the vehicle's transmission system. In some vehicle applications, this design may have to be applied due to various reasons such as the battery pack or the vehicle's center of gravity being off-center.

Available transmission drive systems

The engine power transmission mechanisms of the vehicle to be converted to electric may have to be made on the internal combustion engine transmission in some vehicles due to technical restrictions or design reasons, directly from the electric motor to the vehicle's axles. In this case, the vehicle's existing transmission system is used to transfer the electric motor's power movement to the wheels. In cases where the electric motor does not fit the existing transmission system, installation is provided with interconnect elements. This connection element can be specially prepared depending on the vehicle type, transmission type and electric motor type, or it is also available as a universal converter in ready-made conversion kits. When it is not available in conversion kits, it is added as an additional investment cost.

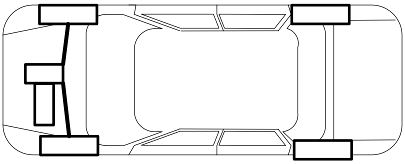

Figure 5. Current Transmission Driven Front Wheel Drive Electric Vehicle Model

The conversion is completed by connecting electric motors to the existing drive system of some vehicles. In such designs, electric motors are connected to the previous transmission equipment of the vehicle with the help of an inverter. The front-wheel drive design in this design is shown in Figure 5.

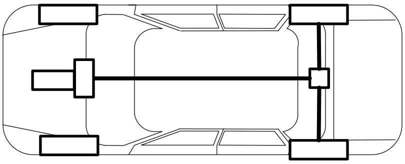

Figure 6. Current Transmission Drive Rear-Wheel Drive Electric Vehicle Model

Due to design constraints, the drive system used in the electric vehicle conversion may have to be implemented as rear-wheel drive. In this case, the application design is made to the vehicle's existing buddy-drive transmission system, as seen in Figure 6.

Unit costs and calculation methods

There are various design models for the conversion of internal combustion fossil fuel vehicle engines to electric vehicles. The calculation parameters to be included in the costs also vary depending on the design models. The total (TM) cost calculation formula to be used in the electric vehicle conversion can be expressed as equation (3).

$$TM = \sum_{i \in I} \sum_{j \in J} SM_i + \omega DM_i^j + \omega BM_i^j \quad \forall i \in I, \forall j \in J, \qquad \omega = \{0,1\} \quad (3)$$

Here, total cost *TM*, fixed cost *SM*, maintenance cost *BM*, *i* indicates the economic life of the vehicle, *j* indicates the main parts of the vehicle and ω is a binary variable indicating whether there is a periodic cost.

SM_i indicates the electric motor, battery system, high voltage system, heat pump, air conditioning systems, brake systems that will be added to the vehicle to be transformed in the *i*. period. In this model, $SM_i=1$ is accepted and indicates the initial investment made in the first period.

ωDM_i indicates the costs incurred in the *i*. period, such as the low voltage system, reducer and connection elements, application unit labour, which are independent of each other. Here, *ω* indicates whether there is a cost in the *i*. period and is calculated as shown in equation (4).

$$\omega DM_i^j = \sum_{i=1}^{10} \sum_{j=1}^{k} dM_i^j \quad i = 1,2,..,10 \; j = 1,2,..,k \; \omega \; ve \; k \in 1,0 \qquad (4)$$

ωBM_i^j This expression showing the maintenance cost shows the total of the maintenance costs that may occur in the *j.th* part in the *i.* period, which are independent from each other but must be done at certain intervals. In general, these costs consist of maintenance in the battery and high voltage system, and the ω parameter shows that the cost will be done in the relevant period.

$$\omega BM_i^j = \sum_{i=1}^{10}\sum_{j=1}^{k} \beta M_i^j \quad i = 1,2,..,10 \; j = 1,2,..,k \quad \omega \in 1,0 \; \beta \in poisson \; (5)$$

The parameter β is the probability of failure or maintenance cost M_i^j that may occur due to the *j.th* part in the *i.* period. This parameter consists of the sum of the failure probability of each *j.th* part, which consists of decimal numbers ranging from 0 to 1, that may occur independently of the *i.* periods. The total failure probability can be calculated from the probability table obtained from Table 3. In other words, in the calculation of the distribution in the probability calculation, the interval values can be added to the model from the values of Table 3. While the exponential distribution is generally preferred for these probabilities for electrical devices, this uniform distribution is preferred for automobile type vehicles. The failure probabilities of each part occur independently of each other. The probability of a failure occurring and the occurrence of another failure not related to this failure are independent events.

RESEARCH FINDINGS

As mentioned before, the power unit of electric vehicles is expressed in kW (kiloWatt), while the power unit of internal combustion fossil fuel vehicles is expressed in HP (Horse Power). Expressing different power units in kW, which is the common power unit, will provide significant results in terms of comparison. Therefore, determining both fuel and power consumption units in kW will ensure that they are evaluated in a common way. In order to express these two power units in common kW, 1 HP = 0.7457 kW is used as the conversion coefficient. The engine power comparison of internal combustion engines and electric vehicles is shown in Table 9. A point to be noted here is that the type of fossil fuel used in internal combustion fossil fuel vehicles is an important variable in determining the engine power. A similar situation varies depending on whether the engine used in electric motors is direct current (DC) or alternating current (AC).
The cost model calculation proposed in this study was made according to the processes to be followed in the vehicle equipment to be used in the

conversion of a 1400cc internal combustion fossil fuel vehicle into an electric vehicle. In order to avoid any power loss in the vehicle to be converted, the power of the electric vehicle design should be at least as much as the power provided by the fossil fuel vehicle. The comparative power and torque amounts of the engines may not be very meaningful unless compared with equivalent vehicles. These calculations depend on many parameters, from the compression ratios of the fuels to the gear reapers of the transmissions. In order to overcome this issue, some preliminary assumptions were made and the experimental formulation was established. In these calculations, the torque and kW calculation of a vehicle with an accepted vehicle weight of 1100 kg was taken as a preliminary assumption.

Table 10. Power Comparison of Electric Vehicles and Internal Combustion Fossil Fuel Vehicles

Vehicle Type	Power of Motor (kW)	Power of Motor (**HP**)	**Explanation**
Electric Vehicle (EV)	50 - 150 kW	67 - 200 HP	Small and medium segment electric vehicles.
Electric Vehicle (EV)	150 - 300 kW	200 - 402 HP	Mid-range to high-end electric vehicles.
Electric Vehicle (EV)	300 - 1000 kW	402 - 1340 HP	Luxury, sports or high-performance EVs.
Internal Combustion Engine (IC**M**)	40 - 70 kW	54 - 94 HP	Small engine city vehicles.
Internal Combustion Engine (IC**M**)	70 - 150 kW	94 - 201 HP	Mid-range vehicles (sedan, hatchback, etc.).
Internal Combustion Engine (IC**M**)	150 - 300 kW	201 - 402 HP	Luxury and sports vehicles.
Internal Combustion Engine (IC**M**)	300 - 600 kW	402 - 804 HP	Luxury and sports vehicles.
Internal Combustion Engine (IC**M**)	600 - 1200 kW	804 - 1609 HP	Super sports cars, hypercars.

Both technologies have their advantages and disadvantages; electric vehicles generally stand out with their lower maintenance requirements and environmentally friendly features, while internal combustion vehicles generally offer longer range and faster refuelling.

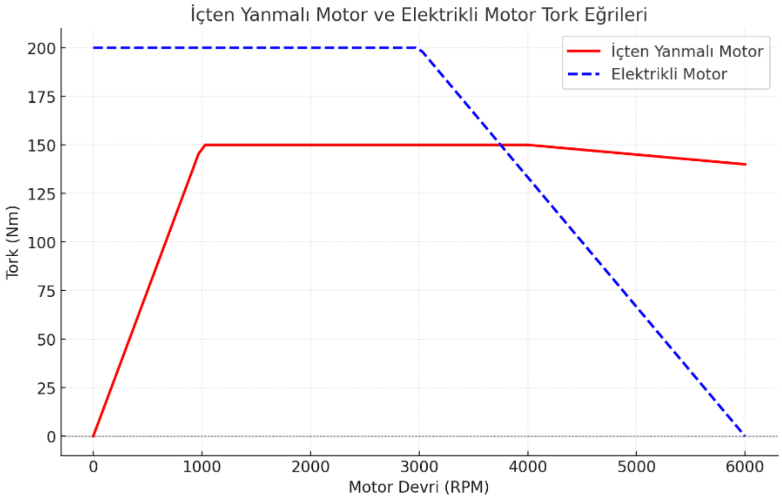

Figure 7. Torque Graph of Electric Vehicle and Internal Combustion Fossil Fuel Passenger Vehicle, (Heywood, 1988a, 1988b; Husain, 2021)

When Figure 7 is examined, it is seen that the torque value observed in the low-speed range of internal combustion engines between 0 and 1000 rpm is low, and as the speed increases between 1000 and 4000 rpm, the torque value increases to a certain point, and then decreases after 5000 rpm. When electric vehicles are examined, it is seen that they produce almost the same amount of torque at a constant level between 0 and approximately 3000 rpm, and decreases after approximately 5000 rpm.
Comparing the electric vehicle conversion compared in terms of the power they consume in terms of costs and calculating the payback period of the investment amount is important in terms of investment profitability. In the conversion of internal combustion vehicles to electric vehicles, how long it will take to amortize the vehicle conversion investment and the investment payback period should be calculated with the break-even point analysis. According to the break-even analysis to be made, it is among the points to be considered in terms of how long it will take to recover the conversion investment and the benefits it will provide.

Table 11. Comparison of Internal Combustion Engine and Electric Passenger Vehicle Torques

Features	**Internal Combustion Engine**	**Electric Motor**
Maximum Torque Range	Mid RPM (2000-4000 RPM)	Instant (from 0 RPM)
Tork **Slope**	Parabolic (rises and falls)	Steady and then drops
Low Speed Performance	Low	Very High
Response Time	Delayed	Instant

The basic initial investment costs in the conversion costs of internal combustion vehicles to electric vehicles can be listed as electric motor, electrical equipment, battery pack and assembly-engineering project services. Although the basic initial investment costs vary depending on the type of vehicle to be converted, its features and the purpose of use, if expressed in USD, they range between approximately 10,000 and 30,000 USD. Among these costs, the electric motor is 1,000-5,000 USD, the electrical equipment is 1,000-3,000 USD, the battery pack is 5,000-15,000 USD and the assembly-engineering project services are 2,000-3,000 USD. In order to evaluate the conversion costs, it is necessary to make a break-even analysis of this investment. This analysis is important for decision makers in terms of knowing how long it will take to return the conversion investment cost. Because decision makers want to know how long it will take to pay back this investment and whether the investment is profitable (Blank & Tarquin, 2008; Leland Blank & Tarquin, 2005).

$$Başa\ baş\ süresi = \frac{Dönüşüm\ maliyeti}{Yıllık\ yapılacak\ tasarruf} \tag{6}$$

Equation (6) can be used to calculate the break-even point for the investment to be made for the conversion of an internal combustion fossil fuel engine to an electric vehicle engine. For example, if the annual fossil fuel cost of an internal combustion vehicle is calculated as 2,000 USD, the annual electricity cost for an electric vehicle is 500 USD, the annual savings are 1,500 USD, and the initial investment cost of the conversion is 20,000 USD, assuming that it is calculated with the help of equation (3), the break-even analysis can be calculated as follows.

Fuel savings = 2000 – 500 = 1500 USD

$$Başa\ baş\ süresi = \frac{20.000}{1500} \cong 13.33\ yıl$$

The graph of the calculated transformation cost over the years is as shown in Figure 8. However, the calculations are not always made according to fixed costs and annual increase rates are also taken into account.

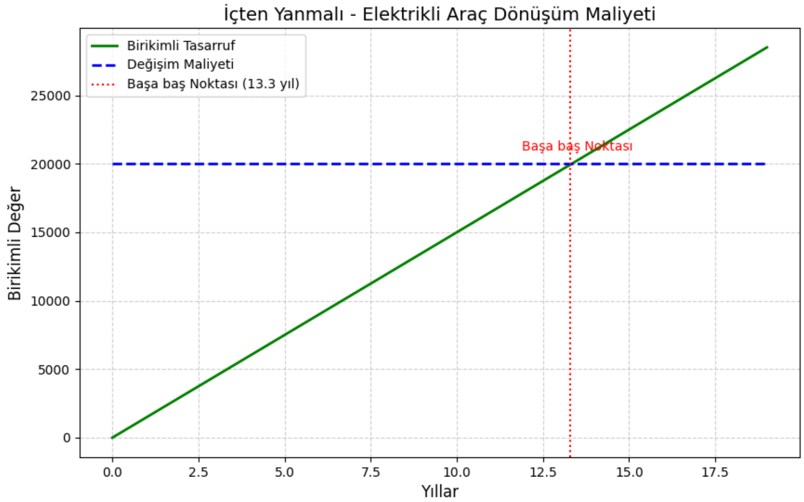

Figure 8. Internal Combustion Engine Electric Vehicle Conversion Cost Break-Even Analysis

In the sample calculation, it was assumed that fuel and electricity prices were fixed. Fuel and electricity prices are not fixed due to some cost increases during the year. In this case, electric vehicle conversion points need to be recalculated according to these variable costs. In this example, if the annual increase in fossil fuel costs is 5% and the electricity increase fee is 3%, the break-even point can be calculated as follows using the cumulative interest formula.

$$A = a\,(1 + r)^n \tag{7}$$

In this formula in Equation (7), where A is the total income to be calculated in n years, r is the increase rate and a is the initial cost, the calculated value is approximately 10 years. The graph of this calculation is as seen in Figure 9.

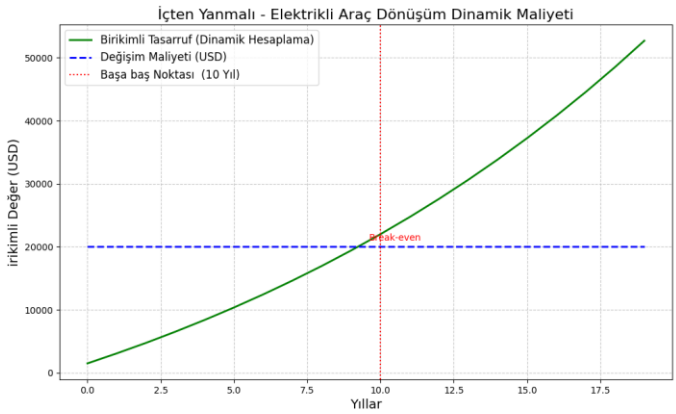

Figure 9. Internal Combustion Engine Electric Vehicle Conversion Dynamic Cost Break-Even Analysis

During the years that vehicles are used, their components wear out and their economic value decreases. If the conversion cost is recalculated with this type of cost that can be collected under depreciation expenses, the break-even point analysis may change, and the annual revaluation rate is ignored in this depreciation calculation.

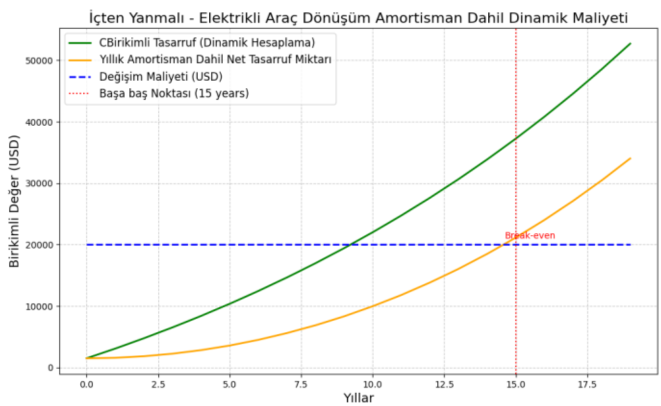

Figure 10. Internal Combustion Engine Electric Vehicle Conversion Dynamic Cost Break-Even Analysis Including Depreciation

When the annual depreciation cost is determined as 10%, the calculated break-even point for the conversion cost of the vehicle is moved further. The main reason for this is the loss of the economic value of the vehicle in the depreciation calculation. The calculated depreciation-inclusive value is shown as 14 years with the orange line in Figure 10. As can be understood from Figure 10, a non-linear relationship is evident between the cost and economic value of the vehicle. The economic return of the conversion costs of the electric vehicle is extended by approximately 4 years due to depreciation expenses. If the depreciation expense rate is selected as high, this return period is extended even further. Considering this situation, it can be concluded that the depreciation cost moves the break-even point forward and the conversion is a long-term investment. According to this table, the experiment was designed by selecting electric motors with equal power and torque values and the calculations were made accordingly. According to these calculations, the specifications of the selected electric motor were determined as 65kW 60Volt 3000 rpm DC.

CONCLUSION ND REMAKS

Electric vehicles have become widespread in the world with the developments they have shown in recent years along with the advancement of technology. Especially when combined with the developments in battery technology and semiconductor technology, it is seen that these developments have accelerated. Internal combustion fossil fuel vehicles have been in human life for almost two centuries since they started to be used in the early 19th century. Developing electrical energy storage systems and green energy movements have started to accelerate the use of electric vehicles in recent years. Climate and geographical changes in the production of fossil fuels, political instability, developing environmental awareness, and socio-economic factors are making the use of electric vehicles even more widespread. Internal combustion vehicles produced over the years are quickly scrapped due to the end of their economic life or the fact that their repair costs have started to reach high amounts. By removing the engine assemblies of internal combustion fossil fuel vehicles from these vehicles and replacing them with electric motors with appropriate equipment and hardware, these scrapped automobiles can be brought back into the economy. In this study, an economic analysis of the conversion of internal combustion fossil fuel vehicles to electric vehicles has been made. As can be seen, it has been seen as a result of the economic analyses that the conversion costs are a long-term investment and that the return on the conversion of internal combustion vehicles to electric vehicles cannot be obtained in the short term. Although the study is a long-term investment, it is a solution to the problems caused by the repair costs of an existing vehicle or the engine becoming unusable due to other reasons. In addition, it can be understood as a result of this study that the emission values released into the atmosphere by internal combustion fossil fuel vehicles can be reduced by converting to electric vehicles. With this transformation, new economic models that will also contribute to sustainable green environmental climate policies can be developed.

REFERENCES

Blank, L. T., & Tarquin, A. J. (2008). *Basics of engineering economy*. McGraw-Hill Higher-Education New York.

Ehsani, M., Singh, K. V, Bansal, H. O., & Mehrjardi, R. T. (2021). State of the Art and Trends in Electric and Hybrid Electric Vehicles. *Proceedings of the IEEE*, *109*(6), 967–984. https://doi.org/10.1109/JPROC.2021.3072788

Hausmann, A., & Depcik, C. (2013). Expanding the Peukert equation for battery capacity modeling through inclusion of a temperature dependency. *Journal of Power Sources*, *235*, 148–158.

Heywood, J. B. (1988a). Combustion engine fundamentals. *1ª Edição. Estados Unidos*, *25*, 1117–1128.

Heywood, J. B. (1988b). Internal combustion engine fundamentals. *(No Title)*.

Husain, I. (2021). *Electric and hybrid vehicles: design fundamentals*. CRC press.

Leland Blank, A., & Tarquin, A. (2005). *Engineering economy*. McGraw-Hill New York.

Liu, P., Wang, J., Hicks-Garner, J., Sherman, E., Soukiazian, S., Verbrugge, M., Tataria, H., Musser, J., & Finamore, P. (2010). Aging mechanisms of LiFePO4 batteries deduced by electrochemical and structural analyses. *Journal of the Electrochemical Society*, *157*(4), A499.

Mi, C., & Masrur, M. A. (2017). *Hybrid electric vehicles: principles and applications with practical perspectives*. John Wiley & Sons.

Okka, O. (2000). *Mühendislik ekonomisi: çözülmüş problemlerle*. Nobel.

OKKA, O. (2019). *Proje Yönetimi ve Mühendislik Ekonomisi [C-5]*.

Yoshio, M., Brodd, R. J., & Kozawa, A. (2009). *Lithium-ion batteries* (Vol. 1). Springer.

Zainuri, F., Sumarsono, D. A., Tullah, M. H., Nuriskasari, I., Subarkah, R., Widiyatmoko, W., Prasetya, S., Susanto, I., & Belyamin, B. (2024). Development electric vehicle conversion to optimization performance. *AIP Conference Proceedings*, *2927*(1).

Evaluation of Hardness, Porosity, Density and Shrinkage Property of Natural Ceramic: High Temperature Effect

Souad GUERFI *[1,2]

[1]Research Center in Industrial Technologies (CRTI), *EChahid Mohammed ABASSI* PB 64, Cheraga, Algiers, Algeria.
[2] Research Advanced Materials Laboratory, Badji Mokhtar University, P .B. 12, Annaba 23000, Algeria.
*guerfisouad@yahoo.fr

ABSTRACT

In this work, the sintering behavior of Algerian natural phosphate raw from the Jebel El Onk region of Tebessa was studied at temperatures ranging from 1000˚C to 1400˚C in air. The effects of temperature on the densification, porosity, shrinkage and Vickers hardness of the raw material were evaluated. Upon heat treatment at 1200˚C, a high density of phosphate was determined while higher temperatures allowed better porosity formation of natural phosphate. Shrinkage measurements are consistent with thermal analysis results. High heat treatment has a positive effect on the hardness of the phosphate grains.

Keywords – Natural Phosphate, Porosity, Density, Sintering Temperature, Bioceramic.

INTRODUCTION

Algeria has abundant and diverse mineral wealth, as its interior is rich in important materials such as iron, feldspar, diatomite, dolomite, quartz, kaolin and phosphates.... Which are used in many industrial fields, such as the environmental field in purifying water from toxic materials such as cadmium and nickel, as well as building materials, ceramics and glass, in addition to catalysts in chemical processes. Algeria has important areas of phosphate in the east of the country in the Tebessa region, and contains a large number of deposits of phosphorous minerals of economic importance, namely the deposits of djebel Kouif, djebel Dir and djebel Onk. Due to its wide uses in several different fields. Recently, phosphate ores have received a great deal of attention due to its important composition represented by fluorideapatite, which is characterized by its good biological properties, biodegradability and stimulates the formation of bone tissue. Natural phosphate is used in the manufacture of bioceramics and glass ceramics. In fact, the present work deals with the study of the thermal behaviour of phosphate ore, extracted from the Kaf El Senoun deposits in djebel Ank (Tebessa), and the evaluation of the effect of sintering temperature on the on the density properties, porosity and shrinkage properties, as well as the hardness, with the aim of exploiting it in the field of bioceramics industry.

MATERIALS AND METHOD

The raw material used in this work is phosphate rock from Kef Essennoun, mining basin of Djebel el Onk (south of Tébessa). A systematic phosphate sampling was carried out at the level of three deposit layers. The blocks were ground using a Fritsch P6 model planetary mill with a 250ml bowl and 13 mm diameter balls for 3h, at a speed of rotation of 350 rpm. The powder obtained is dried at 120˚C using an oven for 24 hours. The samples were sintered at 1000 1100, 1200, 1300 and 1400˚C in a Nabertherm muffle furnace (LHT8/18) in the open air for two hours and a temperature rise rate of 10˚C/min, then ground manually and sieved through a 125µm mesh sieve. Thermal Analysis (TGA / DTA) of natural powder was carried out by TA instruments Q600 SDT), from room temperature to 1300˚C with a temperature ramp of 10˚C/min. The bulk densities of the natural sintered pellets were measured using a helium gas pycnometer (Metromeritics, AccuPyc 1340, USA). The densification and porosity of pellets were measured according to equation (1) and equation (2) respectively, where, d_b is bulk densities and d_t is the theoretical densities. The linear shrinkage (L.S.%) of sintered pellet was determined through the equation (3) [1]. where: D_1 and D_2 represent the diameters of the samples before and after sintering, respectively. Standard Vickers Zwick tester evaluated the Vickers hardness values of the sintered pellets By applying a load of 1 Newton for 10 seconds to the surface of the sample.

$$D = d_b / d_t .100 \qquad (1)$$

$$\varepsilon(\%) = (1 - D)100 \qquad (2)$$

$$L.S = \frac{D_1 - D_2}{D_1} 100\% \qquad (3)$$

RESULTS AND DISCUSSION

A. Thermal analysis

The thermal curves of the raw phosphate are shown in fig.1. Five distinct mass losses can be observed between 50 and 1300˚C for phosphate ores. The initial weight loss of the phosphate was slight, at temperatures below 220˚C, which was due to the dehydration reaction [2-4]. A weak endothermic peak at approximately 86.44˚C in the dta curves accompanied the weight loss. The second and third mass losses occur between 290 and 710˚C, and are significant with an endothermic peak appearing at 683.44˚C on the tda curve; this corresponds to the combustion of organic materials, and the partial carbonization of organic components begins or changes in the material's crystal structure [2, 4, 5]. A significant mass loss was also observed between 720˚C up to 1300˚C. The dta spectrum shows a large endothermic peak located at 789˚C and 1148 ˚C. These peaks can be explained by the total decomposition of the carbonates, metals oxidize and chemical decomposition of phosphate resulting in the formation of a new phase [2-4].

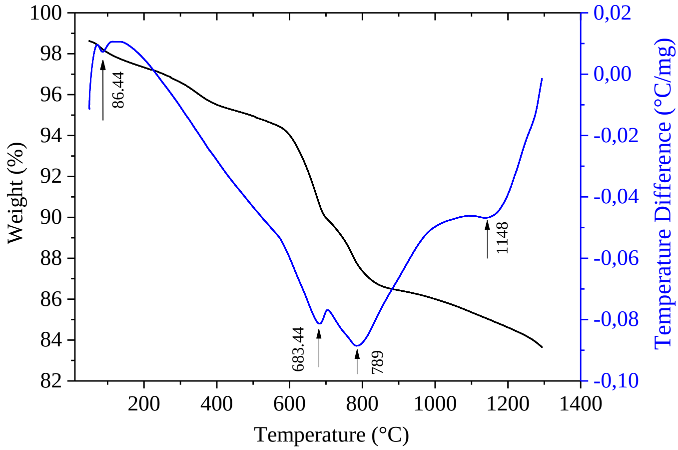

Fig. 1 Thermal analysis (TG/TDA) curves of phosphate ore sample sintered at 1300˚C.

B. Density and porosity analysis

Figure 2 shows the variation of bulk density of the natural phosphate as a function of the sintering temperatures. We can notice that the bulk density of the natural pellet increase with increasing of sintering temperature from 1000 and 1200˚C. The bulk density was 2.65, 2.75 and 2.82 g/cm^3, respectively. For the high temperature range from 1200˚C to 1400˚C, we can observe a decrease in the bulk density from 2.88 to 2.4 g/cm^3 respectively. The variation of porosity and densification curve of the sintered natural bioceramic pellet shows in fig.3. It can be observed that the densification of the samples increases and the porosity of the samples decreases with the increase of the sintering temperature in the low temperatures ranging from 1000˚C to 1200˚C. The densification and porosity values of the samples ranged from 84.12 to 88.88% and from 15.88 to 11.12% respectively. At high temperatures ranging from 1200˚C to 1400˚C, a gradual and regular decrease in the density values was observed, ranging from 88.88 to 76.19%, while the porosity of the samples increased from 11.12 to 23.81%. The change in density and porosity values of the samples by a small percentage of 4% and a slight percentage of

14% at low and high temperatures respectively can be attributed to the formation of crystalline phases, which is responsible for the increase in density and to release of gases outside the sample.

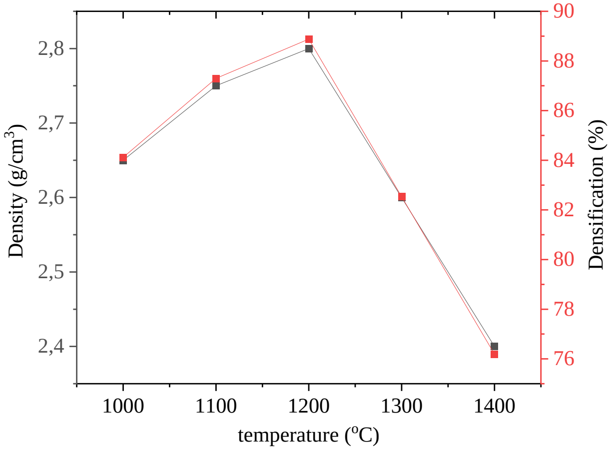

Fig.2 Bulk density curves of sintered bioceramic pellet at different temperature

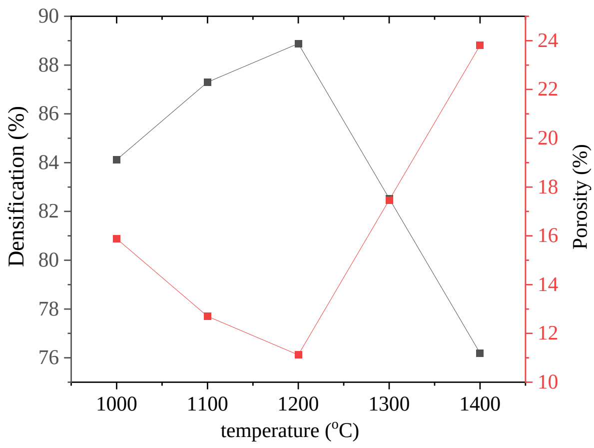

Fig.3 Densification and porosity curves of sintered bioceramic pellet at different temperature

C. Shrinkage measurements

Fig. 4 shows the variation of the shrinkage obtained from the sintered natural bioceramic samples at various temperatures. The shrinkage curve show two different phases; It can be seen that the shrinkage of the samples varies between 9 and 11.12% from 1000˚C to 1100˚C. This increase in shrinkage is generally attributed to the release of CO_2 and SO_3 gases outside the sample and to produce a news oxides phases. From 1100˚C the shrinkage starts to decrease and reaches a value of 10% at 1200˚C. The shrinkage is almost stable between 1200˚C and 1400˚C with an average value of 10.3%. This is due to the partial decomposition of Fluorapatite in β-TCP and CaF_2 and the formation of a new phase crystals. These results are consistent with the thermal analysis results of natural phosphate.

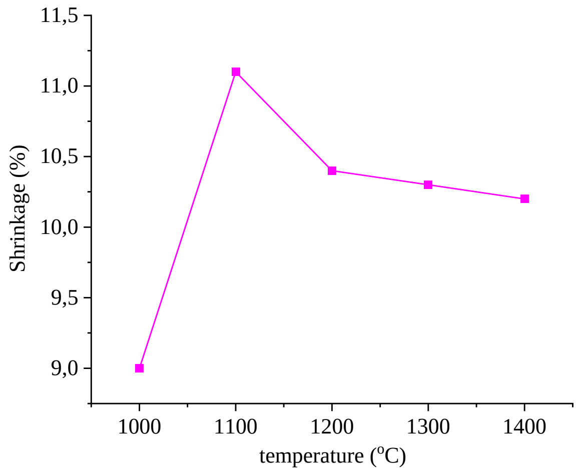

Fig.4 Shrinkage of the samples as a function of the temperature

D. Microhardness analysis

Table 1 shows the measurement of the Vickers hardness of bioceramic samples sintered from 1000 at 1400˚C. The hardness of the natural phosphate samples ranged from 0.71 GPa to 1.29 GPa with increasing sintering temperatures. It can be noted that the effect of sintering temperature on the hardness of phosphate samples is not the same as its effect on the previous properties, density, porosity and shrinkage. The sintering temperature improves the hardness of natural phosphate.

Table 1. The Vickers hardness of natural bioceramic sintered at different temperature.

Temperature (˚C)	1000	1100	1200	1300	1400
Vickers Hardness (GPa)	0.71	0.8	0.89	1.23	1.29

CONCLUSION

In this research, the thermal behavior of algerian mineral phosphate was studied and the effect of high heat treatment on the properties of density, porosity, shrinkage and vickers hardness was investigated. The heat treatment contributed to the weight loss of the prepared phosphate sample as a result of the decomposition of organic matter and the release of carbon and the formation of new materials. The heat treatment at 1400˚C contributed to the occurrence of pores of natural phosphate samples by approximatelyby 24%, with a density estimated at 76 g/cm3. the heat treatment led to differences in the degree of shrinkage, which is consistent with the thermal behavior of phosphate. In addition, high heat treatment allows for better vickers hardness of raw phosphate.

REFERENCES

[1] K. Belhouchet, A. Bayadi, H. Belhouchet, and M. Romero, "Improvement of mechanical and dielectric properties of porcelain insulators using economic raw materials," *boletín de la sociedad española de cerámica y vidrio,* vol. 58, pp. 28-37, 2019.

[2] A.-Z. M. Abouzeid, "Physical and thermal treatment of phosphate ores—An overview," *International journal of mineral processing,* vol. 85, pp. 59-84, 2008.

[3] R. E. K. Billah, F. El Bachraoui, B. El Ibrahimi, H. Abou Oualid, Z. Kassab, G. Giácoman-Vallejos, M. Sillanpää, M. Agunaou, A. Soufiane, and Y. Abdellaoui, "Mechanistic understanding of Nickel (II) adsorption onto fluorapatite-based natural phosphate via Rietveld refinement combined with Monte Carlo simulations," *Journal of Solid State Chemistry,* vol. 310, p. 123023, 2022.

[4] A. Saadoune, "Caractérisation et enrichissement du minerai phosphaté de Djebel Onk (W. TEBESSA)," *Mémoire Magister, École Nationale Polytechnique Département de Génie Minier,* 2010.

[5] M. Loutou, M. Hajjaji, M. A. Babram, M. Mansori, C. Favotto, and R. Hakkou, "Phosphate sludge-based ceramics: Microstructure and effects of processing factors," *Journal of Building Engineering,* vol. 11, pp. 48-55, 2017.

Finite Element Critical Buckling Analysis of Carbon/Epoxy Laminated Composite Plates Under Uniaxial and Biaxial Loading Conditions

Melih SAVRAN*

Department of Mechanical Engineering, İzmir Katip Çelebi University, Turkey
*mlhsvrn@gmail.com

ABSTRACT

Laminated composites are extensively employed in marine, automotive, aerospace, military, and various other engineering applications due to their inherent tailorability, which allows customization to meet specific design requirements. The accurate determination of the buckling load capacity of composite plates under in-plane compressive loads is a critical aspect of designing robust composite structures. This study focuses on evaluating the critical buckling load factor of carbon/epoxy laminated composite plates with 16 and 64 layers, subjected to uniaxial and biaxial loading conditions. The composite plates under consideration are simply supported along all four edges.

The investigation emphasizes the influence of load ratios (Nx/Ny) on the critical buckling load factor. Finite element analyses were conducted using ANSYS 17.2, while analytical computations were performed with Mathematica based on classical lamination plate theory. Comparative assessments of analytical and numerical results were made, including a validation against existing literature. The findings reveal that the critical buckling load values obtained via analytical methods and finite element simulations exhibit high agreement, with discrepancies limited to approximately 3% under identical orientation angles.

For the loading condition LC2 (uniaxial loading, Ny = 1), the critical buckling load factor increases significantly with higher mode numbers. Conversely, the highest critical buckling load factor was observed under LC1 (uniaxial loading, Nx = 1), whereas the lowest was associated with LC5 (biaxial loading, Nx = 1, Ny = 2) for the first buckling mode.

Keywords – Laminated Composite, Buckling Load, Finite Element Analysis, Buckling Mode, Carbon/Epoxy.

INTRODUCTION

Laminated composites are widely utilized in marine, automotive, aerospace, military, and various other engineering applications due to their exceptional mechanical properties, such as high specific modulus (ratio of Young’s modulus to density) and high specific strength (ratio of strength to density). Beyond these attributes, fiber-reinforced composites offer inherent tailorability, including adjustable fiber orientation and stacking sequences, providing significant design flexibility compared to isotropic materials. Key mechanical design considerations for composite structures include deflection, buckling load, resonance frequency, impact resistance, fatigue life, and dimensional stability. Among these, the buckling load capacity under in-plane compressive loads is particularly critical, as buckling often results in premature structural failure. Consequently, maximizing the buckling load has been a primary focus of extensive research.

In this context, Haftka and Le Riche analyzed the buckling behavior of graphite/epoxy symmetric balanced laminated composites under axial and biaxial loading, optimizing stacking sequences to maximize buckling loads while adhering to strain failure constraints [1]. Soykasap and Karakaya studied the buckling load maximization of symmetric laminated composite plates with four-edge simply supported boundary conditions under biaxial compressive loads, employing classical laminated plate theory (CLPT) to model buckling behavior [2, 3]. Deveci et al. introduced a hybrid optimization algorithm combining genetic algorithms and trust region reflective algorithms to determine the optimal stacking sequence for laminated composite plates under puck failure criteria. Their methodology utilized CLPT to define the objective function for optimization [4]. Topal and Uzman addressed both single- and multi-objective optimization for maximizing buckling load and critical temperature capacity, employing first-order shear deformation theory (FSDT) in their formulations while investigating the effects of aspect ratio, lay-up configuration, boundary conditions, and thermal expansion coefficients on buckling behavior [5-7].

The buckling behavior of laminated composite plates is influenced by several parameters, including plate aspect ratio, material properties, ply orientation, and boundary conditions. Complex geometries, in particular, pose challenges for analytical solutions. Experimental methods, while accurate, are often time-consuming and costly. Thus, numerical approaches, particularly finite element methods (FEM), are preferred for the design and analysis of composite structures.

In this regard, Panda and Ramachandra explored the influence of plate aspect ratio, boundary conditions, length-to-thickness ratio, and non-uniform in-plane loading on the buckling behavior of rectangular composite plates without cutouts [8]. Hu and Lin conducted numerical analyses using ABAQUS to study the effects of boundary conditions and circular cutouts on fiber orientation and buckling load for symmetrically laminated composite plates under uniaxial compression [9]. Baba and Baltacı examined the buckling behavior of laminated composite plates with central circular cutouts under uniaxial compression, investigating the effects of anti-symmetric laminate configurations, length-to-thickness ratios, and boundary conditions using ANSYS FEM software [10, 11].

In the present study, the critical buckling load factor of carbon/epoxy laminated composite plates with 16 and 64 layers, and four-edge simply supported boundary conditions, is evaluated under uniaxial and biaxial loading conditions. The effect of load ratios (Nx/Ny) on the critical buckling load factor is analyzed using analytically with Mathematica and numerically finite element software (ANSYS 17.2). The findings contribute to understanding the buckling behavior of laminated composites and provide insights into their design and optimization.

MATERIALS AND METHOD

Finite element critical buckling analysis of carbon/epoxy laminated composite plates under uniaxial and biaxial loading conditions are considered. The elastic properties of carbon/epoxy material gives in Table1.

Table 1. Carbon/Epoxy material mechanical properties [12]

Parameters	Carbon-Epoxy
E_1 Longitudinal modulus (GPa)	181
E_2 Transverse Modulus (GPa)	10.3
G_{12} In-plane shear modulus (GPa)	7.17
V_{12} Poisson ratio	0.28
ρ Material density (kg/m3)	1600

Buckling formulation based on CLPT of laminated composite plate which is four edge simply supported can be defined as [12]

$$\lambda_b = \frac{\pi^2\left[D_{11}\left(\frac{m}{a}\right)^4 + 2\left(D_{12}+2D_{66}\right)\left(\frac{m}{a}\right)^2\left(\frac{n}{b}\right)^2 + D_{22}\left(\frac{n}{b}\right)^4\right]}{N_x\left(\frac{m}{a}\right)^2 + N_y\left(\frac{n}{b}\right)^2 + N_{xy}\left(\frac{m}{a}\right)\left(\frac{n}{b}\right)}$$

where N_x, N_y *and* N_{xy} are normal and shear force, *m* and *n* are half-waves in the x and y directions, respectively, *a* and *b* are length and width of plate and D_{11}, D_{12}, D_{22}, D_{66} are the terms of bending stiffnesses and can be expressed as in the following form

$$D_{ij} = \frac{1}{3}\sum_{k=1}^{N}[(\overline{Q}_{ij})]_k (h_k^3 - h_{k-1}^3),$$

$i, j = 1,2,6$

where h is one ply thickness, N is total play number and $\overline{Q}_{ij}$ is the transformed reduced stiffness matrix.

The values of *m* and *n* are taken to be 1 or 2 in order to result in a good estimate of buckling load capacity. Accordingly, the smallest of λ_b (1,1), λ_b (1,2), λ_b (2,1), λ_b (2,2) yields λ_{cb}

$$\lambda_{cb} = \min \lambda_b(m,n)$$

After obtaining the critical buckling load factor once, critical buckling loads can be determined by means of $N_{x,cr} = \lambda_{cb} N_x$ and $N_{y,cr} = \lambda_{cb} N_y$ expressions.

Finite Element Analysis (FEA)

Buckling analysis of laminated composite plate was investigated utilizing FEM. Carbon/epoxy laminated composite plate under simply supported boundary condition and different load ratios (N_x / N_y) were analyzed using ANSYS Workbench 17.2 finite element software. Figure 1 shows the geometric models and meshes of the laminated composite plate. The meshes were improved utilizing eight-noded shell181 elements, having six degrees of freedom at each node (translations in the nodal x, y, and z directions and rotations about the nodal x, y, and z axes). Finally, a total of 8128 elements and 8320 nodes used, with one elements through the thickness, sixty-four elements through the width and one hundred twenty seven element along the length of the plate. Materials given in Table 1 were utilized in the modal analysis.

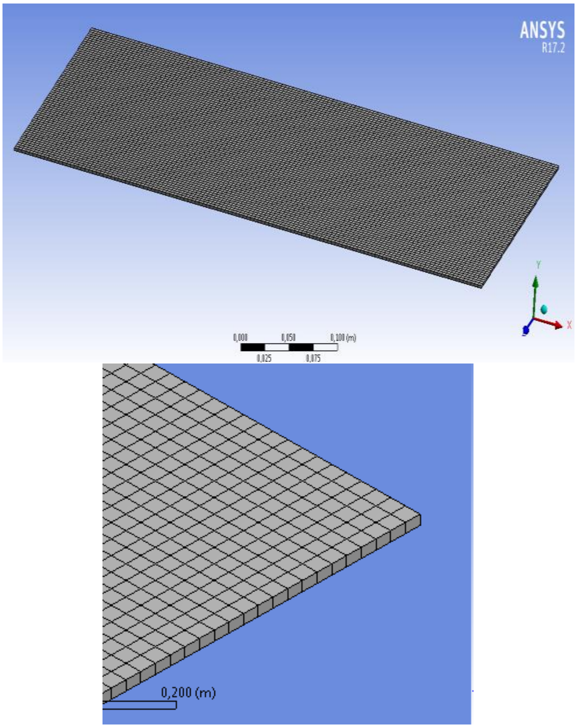

Fig. 1 Material geometry and mesh of finite element model

PROBLEM DEFINITION

Determination of the buckling load capacity of a composite plate under in-plane compressive loads is critical for the design of the composite structures because the buckling could yield a premature failure of the structure. The main goal of this study is to determine the critical buckling load factor of 16 and 64 layered carbon/ epoxy laminated composite plate under uniaxial and biaxial loading conditions. The considered composite plates are simply supported on four sides with length of a and width of b , and subjected to in-plane loads per unit length N_x and N_y as shown in Figure 2.

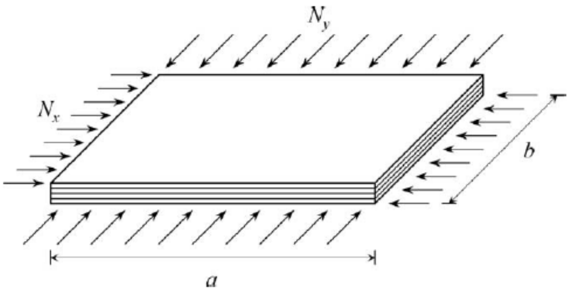

Fig. 2 Laminated composite subjected to in-plane loads [13]

Each layer is 0.127 mm thickness and the width and length of plate equals to 0.254 m and 0.508 m, respectively. N_x has been taken as 1 N/m in the design process. N_y have been calculated from the load ratio (N_x /N_y). The problems including different load cases are given in Table 2.

Table 2. Laminated composite plate load cases

Load case	a (m)	b (m)	N_x (N/m)	N_y (N/m)
LC1	0.508	0.254	1	0
LC2	0.508	0.254	0	1
LC3	0.508	0.254	1	1
LC4	0.508	0.254	1	0.5
LC5	0.508	0.254	1	2

RESULTS AND DISCUSSION

This section presents the results of buckling analyses for various load cases (LC1–LC5) using the Classical Laminated Plate Theory (CLPT) implemented in Mathematica and validated with ANSYS Workbench. The geometrical dimensions of the laminated plates are defined as a=0.508m, b=0.254 m and h=0.000127 m. Table 3 provides the critical buckling load factors for 16-layered and 64-layered carbon/epoxy laminated composites with stacking sequences $[90_2/45/90/45_4]_s$, $[90_6/\pm45_2/90_4/\pm45_2/90_{14}]_s$ and $[\pm45/90_{10}/\pm45/90_2/\pm45/90_2/\pm45/90_{10}]_s$ as computed using ANSYS and Mathematica software. The analysis is based on the CLPT framework, with Load Case 3 (LC3) employed as the reference scenario for designing the composite plates.

The results demonstrate that the critical buckling load factors obtained through analytical calculations and numerical simulations are in close agreement with those reported in the literature [12] for the same orientation angles. This alignment confirms the accuracy and reliability of the Mathematica-based CLPT implementation and the finite element analysis performed using ANSYS 17.2. Both methods provide consistent and validated solutions for the studied benchmark problems.

Table 3. Comparison of critical buckling load factor for 16 layered and 64 layered symmetric carbon/epoxy laminates

Stacking sequence	Λ_{critic} ([12])	Λ_{critic} Mathematica (Present)	Λ_{critic} Ansys (Present)
$[90_2/45/90/45_4]_s$	14673.2	14673.2	14195
$[90_6/\pm45_2/90_4/\pm45_2/90_{14}]_s$	940665	940665	957500
$[\pm45/90_{10}/\pm45/90_2/\pm45/90_2/\pm45/90_{10}]_s$	940665	940665	957500

Figure 3 illustrates the mode shapes of a 64-layer symmetric carbon/epoxy composite plate under biaxial compressive loading, analyzed for two stacking sequences: $[90_6/\pm45_2/90_4/\pm45_2/90_{14}]_s$ and $[\pm45/90_{10}/\pm45/90_2/\pm45/90_2/\pm45/90_{10}]_s$. The mode shapes predominantly appear along the plate's longitudinal direction, attributed to the high length-to-width ratio. Notably, the mode shapes remain consistent across the different stacking sequences, indicating that the stacking configuration does not significantly influence the mode shape under these loading conditions.

	Mode 1	**Mode 2**	**Mode 3**	**Mode 4**
$[90_6/\pm45_2/90_4/\pm45_2/90_{14}]_s$	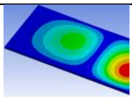	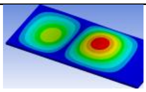	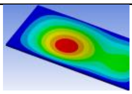	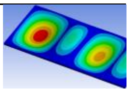
$[\pm45/90_{10}/\pm45/90_2/\pm45/90_2/\pm45/90_{10}]_s$	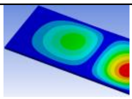	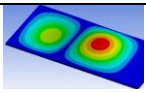	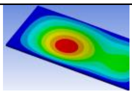	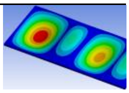

Fig. 3 Mode shape of 64 layered symmetric carbon/epoxy composite plate

Table 4 shows the effect of different loading condition on critical buckling load factor for 16 layered carbon/epoxy laminate for $[90_2/45/90/45_4]_s$ stacking sequence.

Table 4. The effect of different load condition on critical buckling load factor for 16 layered carbon/epoxy laminate

Stacking sequence	Load case	a (m)	b (m)	N_x (N/m)	N_y (N/m)	Λ_{critic} Mathematica	Λ_{critic} Ansys
	LC1	0.508	0.254	1	0	29346.4	29991
	LC2	0.508	0.254	0	1	18393.4	18861
$[90_2/45/90/45_4]_s$	LC3	0.508	0.254	1	1	14673.2	14195
	LC4	0.508	0.254	1	0.5	19564.3	19026
	LC5	0.508	0.254	1	2	8174.87	8110.4

The critical buckling load factor is observed to vary within the range of 29346.4 to 8174.87. The highest value is achieved under uniaxial loading conditions (LC1), while the lowest value corresponds to the biaxial loading condition (LC5). Across all cases, the results obtained from the CLPT-based Mathematica code and ANSYS finite element analysis exhibit strong agreement, with a deviation of approximately 3% between analytical and numerical analyses. Figures 4 and 5 provide a comprehensive overview of the critical buckling load factor values and corresponding mode shapes for each loading scenario (LC1–LC5), offering detailed insights into the buckling behavior under different loading conditions.

Figure 4 clearly demonstrates that the critical buckling load factor for LC2, corresponding to uniaxial loading (Ny=1), exhibits a rapid increase with rising mode numbers. In contrast, the other load cases display a more gradual increase in critical buckling load factors as the mode number increases, indicating distinct buckling behaviors.

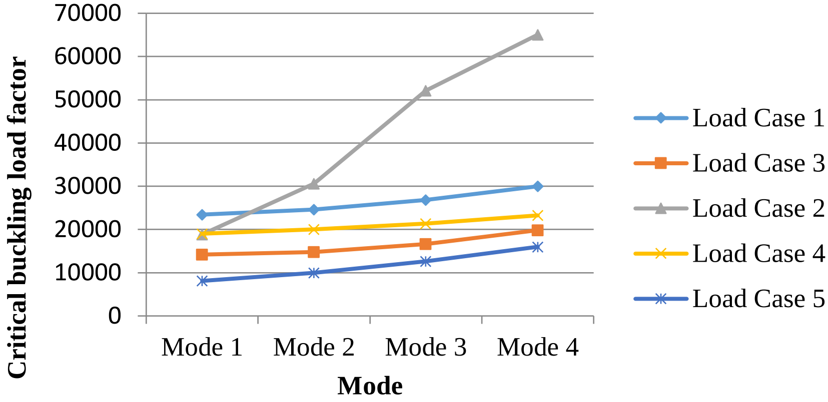

Fig. 4 Effect of load ratio on the critical buckling load factor of 16 layered carbon/epoxy plate

An analysis of Figure 5 reveals that identical mode shapes occur for LC3 and LC5, suggesting a similar deformation pattern under these loading conditions. Additionally, the mode shapes for LC1 are consistent across different mode numbers, indicating a stable and uniform buckling behavior specific to this loading scenario. These observations highlight the influence of loading conditions on the buckling characteristics of laminated composite plates.

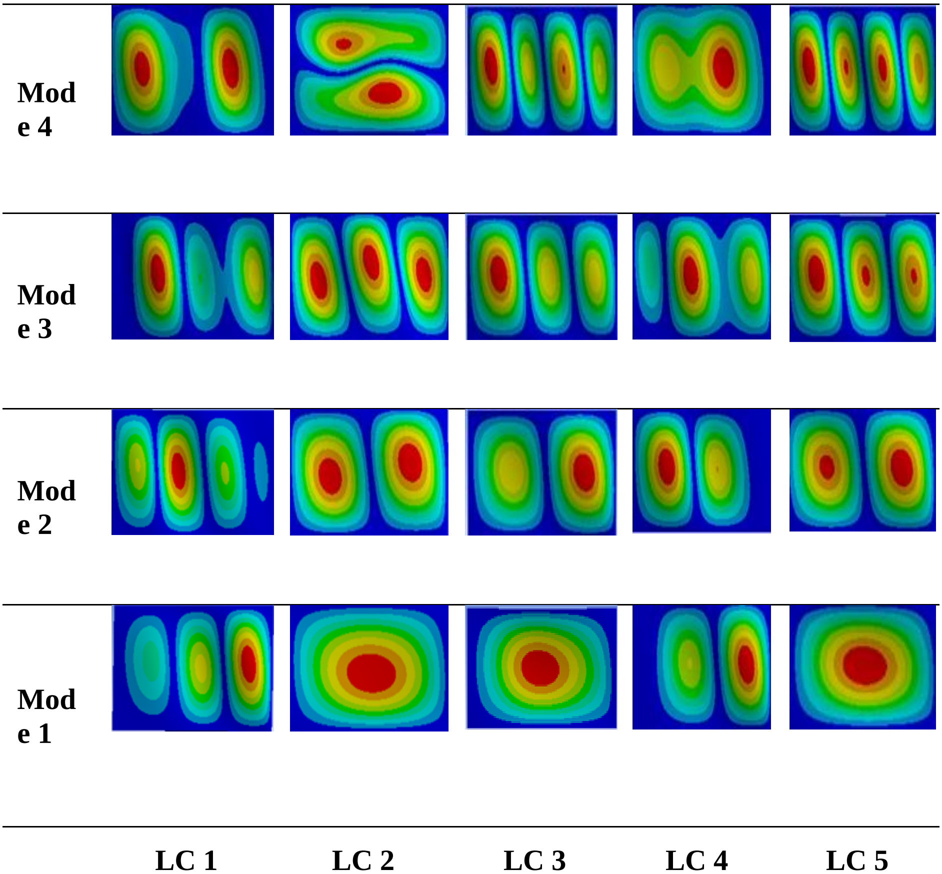

Fig. 5 Effect of load ratio on mode shape of 16 layered symmetric carbon/epoxy plate

CONCLUSION

This study investigates the critical buckling load factor of carbon/epoxy laminated composite plates with 16 and 64 layers, subjected to uniaxial and biaxial loading conditions. The plates are assumed to have four-edge simply supported boundary conditions. The influence of load ratios (Nx/Ny) on the critical buckling load factor is systematically analyzed. The design and analysis of the composite plates are performed using Mathematica and ANSYS 17.2 finite element software.

The results demonstrate that the critical buckling load values obtained through analytical calculations and finite element simulations are in close agreement, with a deviation of approximately 3% for the evaluated orientation angles. For the uniaxial loading condition represented by LC2

(Ny = 1), the critical buckling load factor exhibits a rapid increase with higher mode numbers. Among the investigated cases, the highest critical buckling load factor is observed under the uniaxial loading condition LC1, while the lowest value is recorded for the biaxial loading condition LC5 under mode 1. These findings provide valuable insights into the buckling behavior of laminated composite plates under various loading scenarios.

REFERENCES

[1] Haftka, R. T., & Le Riche, R. (1993). Optimization of laminate stacking sequence for buckling load maximization by genetic algorithm. *AIAA J,* 31(5), 951-956.

[2] Karakaya, Ş., & Soykasap, Ö. (2009). Buckling optimization of laminated composite plates using genetic algorithm and generalized pattern search algorithm. *Structural and Multidisciplinary Optimization*, 39, 477-486.

[3] Soykasap, Ö. and Karakaya, Ş., 2007, Structural Optimization Of Laminated Composite Plates For Maximum Buckling Load Capacity Using Genetic Algorithm. *Key Engineering Materials*. 348-349, 725-728.

[4] Deveci, H. A., Aydin, L., & Seçil Artem, H. (2016). Buckling optimization of composite laminates using a hybrid algorithm under Puck failure criterion constraint. *Journal of Reinforced Plastics and Composites*, *35*(16), 1233–1247. https://doi.org/10.1177/0731684416646860

[5] U. Topal, U Uzman. (2007). Optimum design of laminated composite plates to maximize buckling load using MFD method, *Thin-Walled Structures*, 45 (7–8), 660–669.

[6] U. Topal, U. Uzman. (2010). Thermal buckling load optimization of laminated composite plates, *Thin-Walled Structures*, 46, 667–675.

[7] U. Topal, U Uzman. (2010). Multiobjective optimization of angle-ply laminated plates for maximum buckling load, *Finite Elements in Analysis and Design*, 46, 273-279.

[8] Panda S K and Ramachandra L S. (2010). Buckling of rectangular plates with various boundary conditions loaded by non-uniform inplane loads. *International Journal of Mechanic Science,* 52, 819–828

[9] Hu H-T and Lin B-H. (1995). Buckling optimization of symmetrically laminated plates with various geometries and end conditions. *Composite Science & Technology,* 55, 277–285.

[10] Baba B. O. (2007). Buckling behaviour of laminated composite plates. *Journal of Reinforced Plastics and Composites,* 26, 1637–55.

[11] Baba B. O., & Baltaci A. (2007). Buckling characteristics of symmetrically and antisymmetrically laminated composite plates with central cutout. *Applied Composite Materials,* 14, 265–276.

[12] Karakaya, S., & Soykasap, O. (2011). Natural frequency and buckling optimization of laminated hybrid composite plates using genetic algorithm and simulated annealing. *Structural and Multidisciplinary Optimization*, *43*, 61–72. https://doi.org/10.1007/s00158-010-0538-2

[13] Lopez, R. H., Luersen, M. A. and Cursi, E. S., 2009, Optimization of laminated composites considering different failure criteria. *Composites: Part B*, 40, 731-740.